studeersnel

RWA Assignment 1 Group 1 Report

Rotor / wake Aerodynamics (Technische Universiteit Delft)

Scan to open on Studeersnel

AE4135 ROTOR / WAKE AERODYNAMICS

Wind Turbine Blade Element Momentum
Group 1

Nils Joseph Gaukroger	5319188
Mathieu Pellé	4650077
Guillem Vergés i Plaza	5274281

Delft, the Netherlands

March 25, 2021

Contents

Nomenclature

Abbreviations

BEM	Blade element momentum
BEMT	Blade element momentum theory
TE	Trailing edge
TSR	Tip speed ratio

Greek symbols

α	Angle of attack	[°]
β	Twist angle	[°]
Γ	Circulation	$[\mathrm{m\,s^{-2}}]$
γ	Yaw angle	[°]
λ	Tip speed ratio	[-]
μ	Non-dimensional radius $\left(\frac{r}{R}\right)$	[-]
ω	Rotational velocity	$[\mathrm{rad\,s^{-1}}]$
ϕ	Inflow angle	[°]
Ψ	Azimuthal position	[°]
ρ	Density	$[\mathrm{kg\,m^{-3}}]$
σ	Solidity	[-]
θ	Pitch angle	[°]
θ_g	Global pitch angle	[°]

Roman symbols

a	Axial induction	[-]
a'	Azimuthal induction	[-]
B	Number of blades	[-]
c	Chord length	[m]
C_d	Drag coefficient	[-]
C_l	Lift coefficient	[-]
C_n	Axial force coefficient	[-]
C_P	Power coefficient	[-]
$C_P(r)$	Local power coefficient	[-]
C_Q	Global torque coefficient	[-]
$C_Q(r)$	Local torque coefficient	[-]
C_T	Global thrust coefficient	[-]
C_t	Azimuthal force coefficient	[-]
$C_T(r)$	Local thrust coefficient	[-]
F	Prandtl correction factor	[-]
f_n	Axial loading	$[\mathrm{N\,m^{-1}}]$
f_t	Azimuthal loading	$[\mathrm{N\,m^{-1}}]$
h_0	Stagnation enthalpy	$[\mathrm{J\,kg^{-1}}]$
p	Static pressure	[Pa]
R	Total blade radius	[m]
r	Radial position	[m]
U_∞	Wind velocity	$[\mathrm{m\,s^{-1}}]$
V	Resultant velocity	$[\mathrm{m\,s^{-1}}]$
V_n	Axial velocity	$[\mathrm{m\,s^{-1}}]$
V_t	Azimuthal velocity	$[\mathrm{m\,s^{-1}}]$

1 Introduction

This report, produced as evidence of the first group assignment of the course "Rotor / Wake Aerodynamics" at TU Delft, makes use of the *Blade Element Momentum* (BEM) *theory* model in evaluating the performance of an extracting turbine on the basis of its mechanical and geometric parameters as well as the characteristics of the interacting flow. The model results from the theories: the *Blade Element Theory* and the *Momentum Theory*. Ledoux et al. [1] gives a very good background to these theories and their amalgamation into BEM.

The former theory was introduced by Froude [2] in 1878 to study the behaviour of turbines from a local point of view. In this framework, the turbine blade is discretised into sections, the *blade elements*, each of which are approximated using strip theory as 2D aerofoils. This approach results in expression for the forces exerted on the blade element, as functions of the flow characteristics and blade geometry. The fundamental quantities of this model are two experimental coefficients, the *lift* and *drag coefficients*, C_l and C_d, given for the single aerofoil in question in this report in section 3. These account for the for the forces on the aerofoil as functions of *angle of attack*, α. The forces on the aerofoil are then integrated numerically over the whole radius of the blade to obtain global values.

The Momentum Theory, also known as *Disk Actuator Theory* or *Axial Momentum Theory*, was introduced by William J. M. Rankine in 1865 [3] and is, unlike Blade Element Theory, a global theory that adopts a macroscopic point of view to model the behaviour of a *streamtube* of fluid passing through a turbine. This approach was later taken up independently by Frederick W. Lanchester [4], Albert Betz [5], and Nikolay Joukowsky [6] to formulate *Betz's Law*, which gives the theoretical limit on efficiency of a thin rotor [7]. In 1926, Hermann Glauert combined the locally focused Blade Element Theory with the globally focused Momentum Theory and, accounting also for the rotation in the wake, produced Blade Element Momentum Theory [8].

As mentioned, although the BEM model is applied to a wind turbine in this case, it can also be applied to propelling turbines such as those used on aircraft or helicopters. BEM theory has seen remarkable longevity, partly due to the relative simplicity of the approach compared with the complex phenomena that are developed in the coupled turbine/fluid system. Although there have been corrections, such as Prandtl's tip loss correction, explained in section 4, and other models proposed, such as Joukowsky's model [9], as pointed out in [10]:

"Blade element momentum theory continues to be widely used for wind turbine applications such as initial aerodynamic analysis, conceptual design, loads and stability analysis, and controls design."

The following report is then structured as follows: Section 2 provides a outline of the code used to implement the BEM model, followed by statement and discussion of the major assumptions involved in BEM and its implementation. Section 3 then describes the characteristics of the aerofoil used in this assignment and their implications on the blade design. This is followed by a brief explanaion of the Prandtl tip and root corrections and their implementation within the BEM model in Section 4. Section 5 then outlines the process of choosing a mesh for the discretisation of the blade, presents a sensitivity analysis, and discusses the relative merits of the potential spacing methods. Section 6 then presents results for the non-yawed (axial) flow case in the form of spanwise distributions of angle of attack, inflow angle, axial and azimuthal inductions, and axial and azimuthal force coefficients. All plots will be given for three tip-speed ratios ($\lambda = 6, 8, 10$) and global thrust and torque coefficients will also be presented, as well as spanwise distributions of stagnations enthalpies at four positions within the streamtube. Section 7 provides the same parameters, but this time for the yawed inflow case, and therefore also explains the effects of yaw on these parameters. Section 8 then covers an example of an optimisation method using BEM to maximise performance of a rotor for a fixed design thrust coefficient of $C_{T,design} = 0.75$ and compares the design to the original design from Sections 1 - 7. Finally, Section 9 provides a short conclusion, including the similarities and differences between the two rotor configurations, flow field and operation.
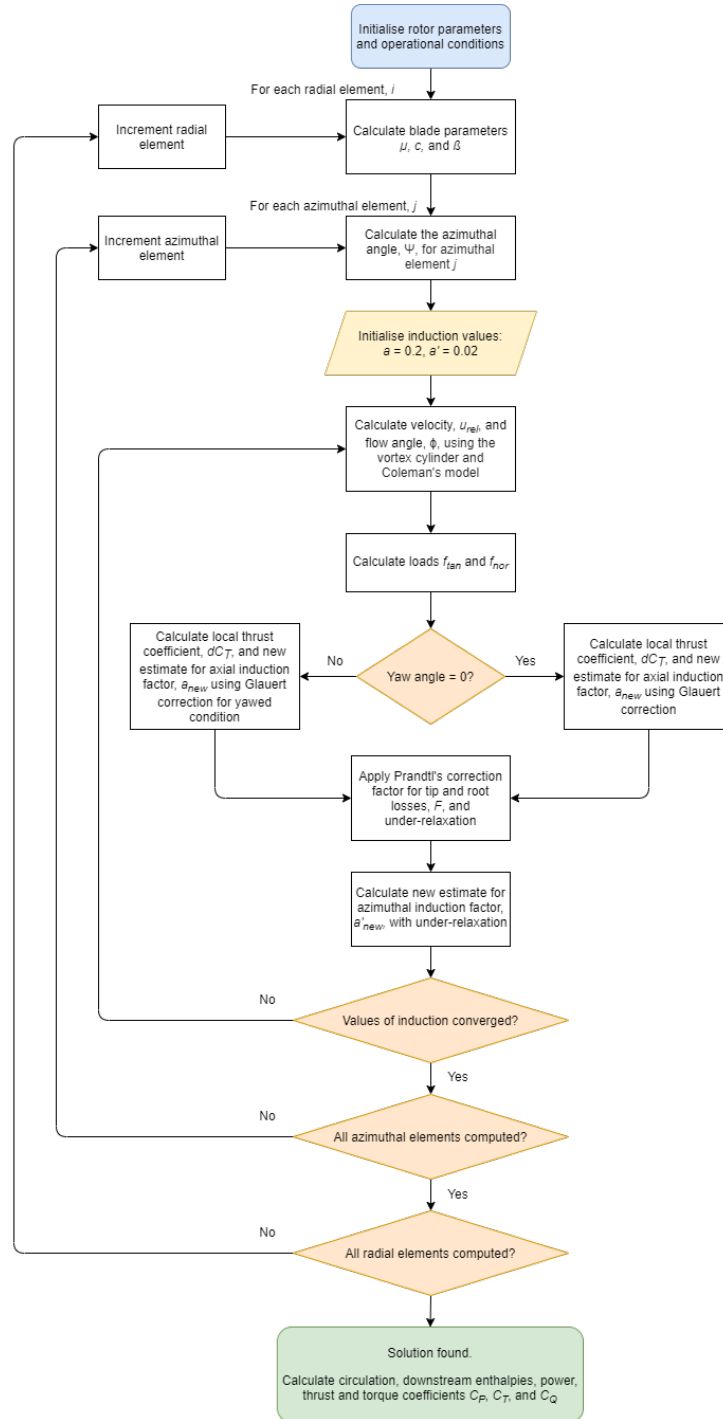
2 Code Outline

2.1 Flowchart

Figure 1: Flowchart for BEM code.

2.2 Assumptions

- The flow is steady, all time derivatives disappear from the continuity momentum and energy equations.

The classical blade element momentum method assumes the inflow to be steady, and is therefore useful for calculating steady loads or power curves such as to predict the annual energy production of a wind turbine. However, in reality the wind incident on a wind turbine rotor is inherently unsteady, due to for example atmospheric turbulence, wind shear and the presence of the tower. There exists therefore also an *unsteady* BEM method, which accounts for this [11].

- The flow is inviscid, the action of viscous forces and viscous diffusion are negligible.

Real flows are not inviscid, but given the vicosity of air is relatively low and the majority of the relevant forces are pressure forces not viscous forces, this is a reasonable assumption. However, it is notable that the aerofoil polars are not derived from inviscid analysis.

- The flow is assumed incompressible and constant-density, and so the continuity equation simplifies to the divergence-free condition.

Again, real flows are not incompressible, but given the low Mach numbers involved, and the relatively small variations in temperature, the density variation can be considered negligible. There can be cases where this is difficult however, for example in unstable atmospheric stabilities, but these are more likely to be analysed using CFD.

- The fluid is assumed to have constant internal energy, there is no flow of heat or work into or out of the fluid, simplifying the energy equation.

For the case of a wind turbine, this is also a reasonable assumption.

- The energy equation can be simplified to the Bernoulli equation.

The previous assumption of constant internal energy then allows the energy equation to be simplified and therefore for the regions either side of the actuator disk, one can apply the Bernoulli equation.

- There is a sufficient number of blades on the rotor for every fluid particle passing through the rotor disc to interact with a blade, that is, all fluid particles undergo the same loss of momentum.

This assumption will be addressed by the Prandtl corrections in 4.

- The actuator disk can be discretised into annular radial elements, which can be solved solved independently.

The basic assumption of BEM theory is that the force of a blade element is solely responsible for the change of axial momentum of the air which passes through the annulus swept by the element. It is, therefore, to be assumed that there is no radial interaction between the flows through contiguous annuli; a condition that is, strictly, only true if the axial flow induction factor does not vary radially. In practice, the axial induction factor is seldom uniform, but experimental examination of flow through propeller discs by Lock et al. [12] shows that the assumption of radial independence is acceptable [13].

TUDelft

3 Aerofoil Operational Point

In this section the polars curves of the airfoil will be described. Two possible design points of the airfoil will be analysed. The implications of the selected C_l and C_d on the blade design will be also discussed.

The next figures show the polar curves of the DU95-W-180 airfoil, which is used in all the blade span in both the original and the re-designed geometries. It is a thin airfoil designed by TU Delft for a Reynolds number of $3 \cdot 10^6$, with a smooth stall behaviour, and a high efficiency, specially in its clean configuration. It has a thin TE to reduce the generated noise, which makes it more favourable its usage in the outer sections of the blades. [14]

When selecting the design operational point for the new design, which will be carried out in the section 8, there are two common approaches [15]:

1. $C_{l,des} = C_l(E_{max})$: Design lift coefficient selected such that the maximum efficiency is achieved.

2. $C_{l,des} = C_{l,max} - 0.4$: Design lift coefficient selected based on a distance from maximum lift coefficient.

The first approach ensures that the viscous losses will be minimised. However, this design point may be too close to the stall angle of attack. The second approach guarantees a sufficient distance to the stall point. The latter method is usually preferred in real designs to achieve a more solid and consistent solution [15]. Both points are shown in the polar plots below with a black and a red cross respectively.
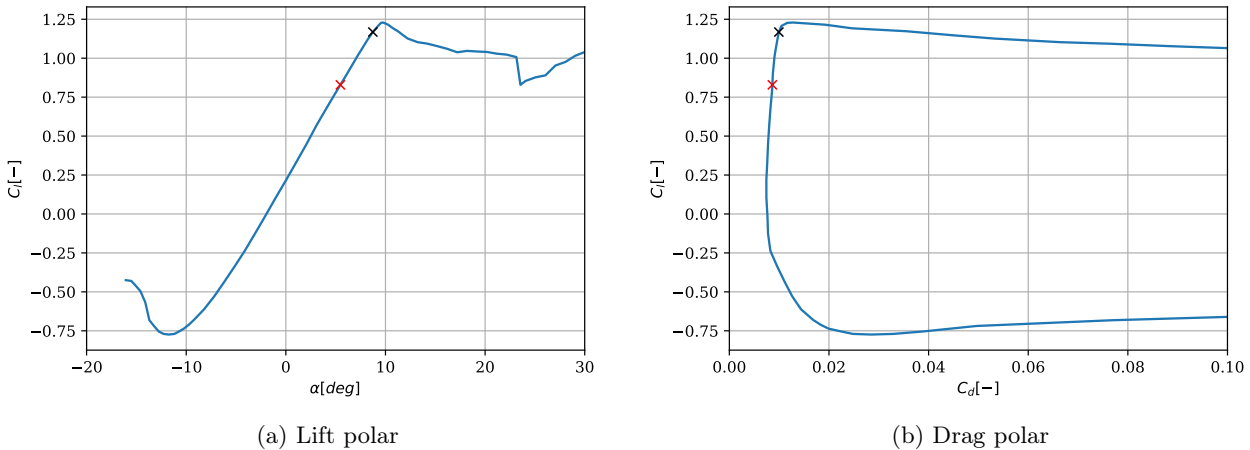

(a) Lift polar

(b) Drag polar

Figure 2: DU 95-W-180 aerofoil polars.
Black cross indicates $C_{l,des} = C_l(E_{max})$. Red cross, $C_{l,des} = C_{l,max} - 0.4$.

The approach selected for the optimisation (section 8) will be the first one, because the loads and structural requirement are not taken into account. It is desirable to maximise C_l/C_d in order to maximise the power coefficient. Another consequence of choosing the black point is that the selected chord would be smaller than in the red cross case. A higher lift coefficient requires a smaller chord to have the same performance. This can clearly be observed looking at the equation 3.69a of the *Wind Energy Handbook* [13]:

$$\sigma \lambda C_l = \frac{8/9}{\sqrt{\left[1 - \frac{1}{3}\right]^2 + \lambda^2 \mu^2 \left[1 + \frac{2}{9\lambda^2 \mu^2}\right]^2}} \tag{1}$$

This equation has been obtained by maximising the torque produced at each blade station and neglecting the drag. It is demonstrated that drag has very little effect in the blade geometry, as seen in the Figure 3.24 of the

same reference. The left hand side of the equation is usually called blade geometry parameter. The solidity is defined as $\sigma = cB/2\pi r$. Therefore, for a design tip speed ratio and a given radius μ, the chord and lift coefficient are related as $C_l \cdot c = K$. The constant K should be maintained to ensure the optimal geometry, and hence an increase of the design lift coefficient would imply a reduction of the needed chord.
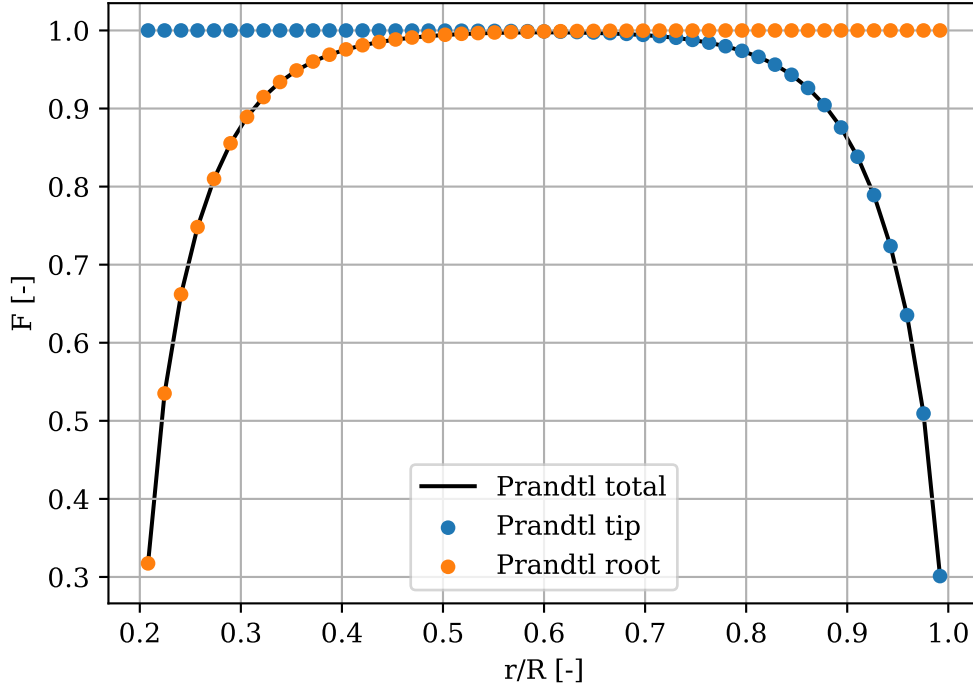
4 Prandtl Tip and Root Corrections

Figure 3: Prandtl tip and root correction factors across blade radius

As stated in subsection 2.2, classical blade element momentum theory is derived based on the assumption of an infinite number of blades, such that all fluid particles passing through the actuator disc experience the same loss of momentum. With a small number of blades however, some fluid particles with interact with them, but most will pass between the blades and, clearly, the loss of momentum by a particle will depend on its proximity to a blade as the particle passes through the rotor disc. If the axial induction factor is large at the blade position then the inflow angle will be small and the torque and, by extension, power will be reduced. This is called the tip-loss effect as it occurs at the outermost part of the blades, however, it also can be shown to occur at the root.

A result of the vortices shed at these two points, the tip and root losses can be quantified using Prandtl's tip and root loss corrections. Independently these are given by Equations 2 and 3 below,

$$F_{tip} = \frac{2}{\pi} \arccos\left(e^{\left(-\frac{B}{2}\left(\frac{1-\mu}{\mu}\right)\sqrt{\left(1+\frac{\lambda^2\mu^2}{(1-a)^2}\right)}\right)}\right) \quad (2) \quad F_{root} = \frac{2}{\pi} \arccos\left(e^{\left(-\frac{B}{2}\left(\frac{\mu-\mu_{root}}{\mu}\right)\sqrt{\left(1+\frac{\lambda^2\mu^2}{(1-a)^2}\right)}\right)}\right) \quad (3)$$

where $\mu = r/R$ and μ_{root} is the location of the root vortex. The tip and root effect are combined in a total correction $F_{total} = F_{tip} * F_{root}$ as shown in Figure 3. This is then applied to the induction values to give corrected induction values $a = \frac{a}{F_{total}}$ and $a' = \frac{a'}{F_{total}}$.

The effect of the Prandtl losses is now shown using the case of $\lambda = 8$ with no yaw misalignment. To have a global figure, it is interesting to note that the power coefficient is reduced from 0.476 to 0.448 (around 6%). Firstly, the axial induction factor may be plotted, and the result obtained clearly shows the opposite shape as the correction factor F shown below:
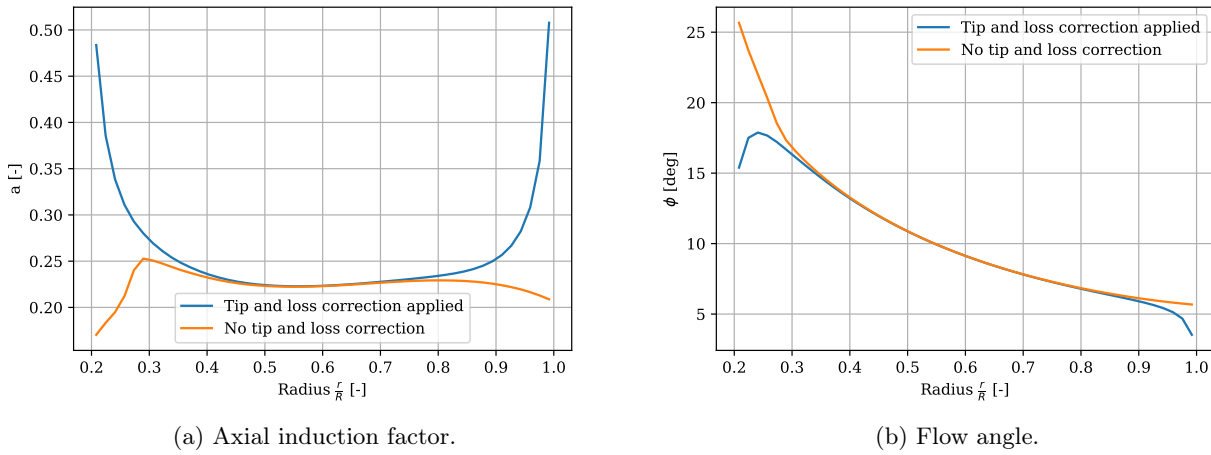

(a) Axial induction factor.

(b) Flow angle.

Figure 4: Axial induction factor and flow angle with and without tip and loss correction.

The preceding figure also shows the flow angle ϕ. The flow angle decreases where the Prandtl correction plays a role. In Figure 5 the effect that this has on the angle of attack is also shown. For the tip, the reduction of angle of attack will imply that the airfoil is operating in a less optimal point (reduced C_l and C_l/C_d). However, in the root the blade without correction is actually in the stall region. This is not very important, because the root has a lower contribution to the total torque. In the tip this is translated to a quite lower tangential force. The torque produced by the outermost sections of the blade will be therefore much lower than in the non-corrected case.
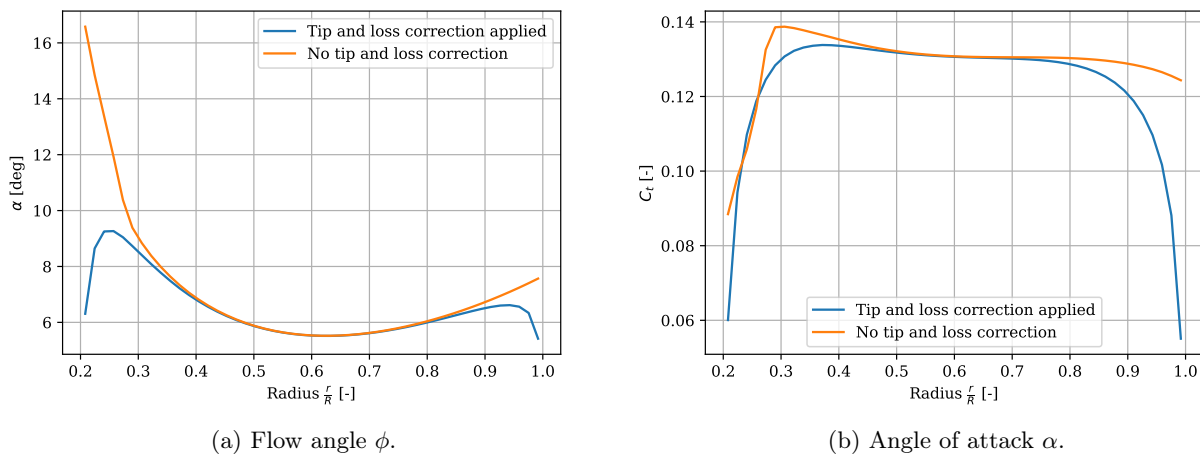

(a) Flow angle ϕ.

(b) Angle of attack α.

Figure 5: Angle of attack and tangential force coefficient with and without tip and loss correction.

5   Mesh Sensitivity Analysis

In this section the selection of the required mesh will be presented. Two different spacing methods have been tested: linear and cosinusoidal, and the effect on time and accuracy of increasing the number of elements has been analysed for each of them.

In the next plot, the execution time and C_T obtained are presented for increasing number of radial elements. The calculations have been performed with the original rotor, at $\lambda = 8$ and no yaw misalignment. The relative error is calculated as:

$$err = \frac{C_T - C_{T,\text{finest mesh}}}{C_{T,\text{finest mesh}}} \tag{4}$$

The number of points required to obtain a relative error of 0.1% will be also calculated. The results are presented in the following figure:
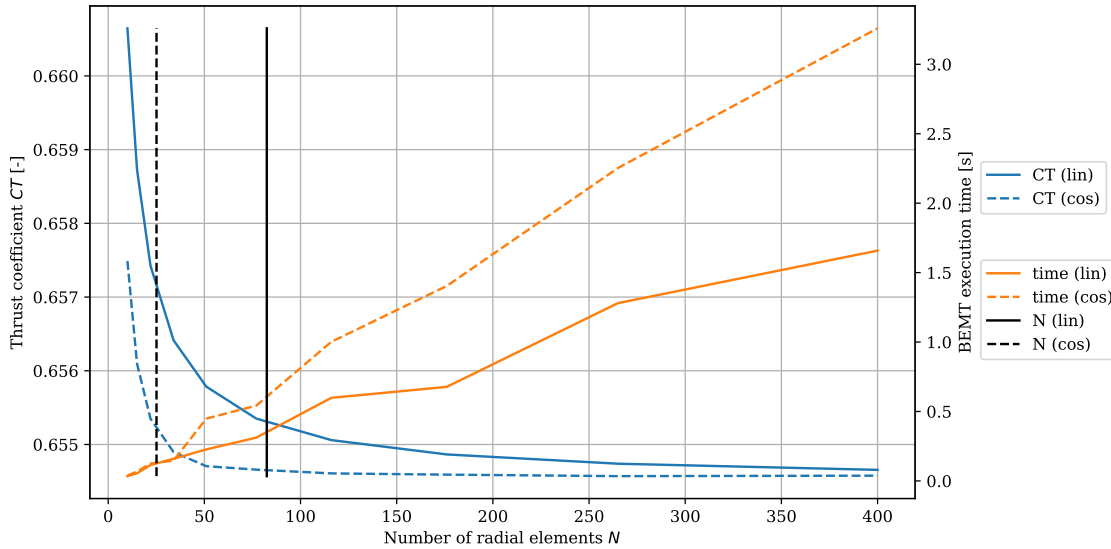

Figure 6: Thrust coefficient and BEMT execution time as a function of the number of radial elements and spacing method. The number of elements required to have a relative error of 0.1% is indicated with black vertical lines.

The first conclusion is evident: the cosinusoidal spacing converges quicker and has smaller errors with the same number of elements. The drawback, however, is a higher computational time, basically given by the fact that points near the root and the tip take more iterations to converge. Although the computational time is very small for a single calculation, one should consider that this steady BEMT is usually the basis for a more complex and complete code. This code could be made unsteady and be coupled with an structural and a control module. These kind of aero-servo-elastic simulations are what is commonly used in the industry to run loads, and a full set of simulations may need to run hundreds of thousands of time-series (hence, millions of single BEMT calculations). Therefore, it is actually important to reduce the computational time at this step.
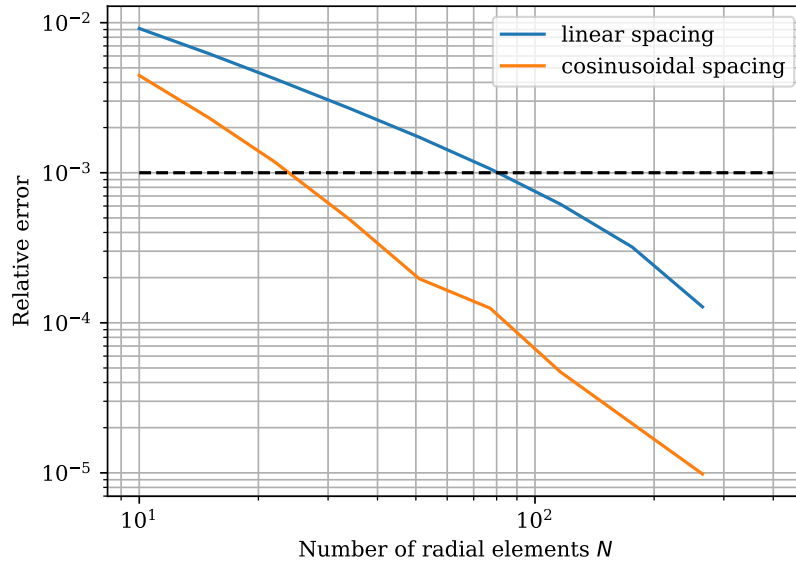
Figure 7: Convergence story as a function of the number of radial elements and spacing method.

The convergence story shows clearly that the order of the cosinusoidal spacing is higher than the linear spacing, and the error reduces more quickly. Going for an error lower than 10^{-5} would not make sense, because it would be in the order of magnitude of the convergence criteria used for each BEMT iteration, therefore the accuracy would be already lost. Besides, the blade element momentum theory is a low-fidelity calculation, so going for a extremely low relative error would be also incoherent with its conceptual purpose.

6   Non-Yawed Rotor Results for Varying Tip Speed Ratios

6.1   Angle of attack and inflow angle

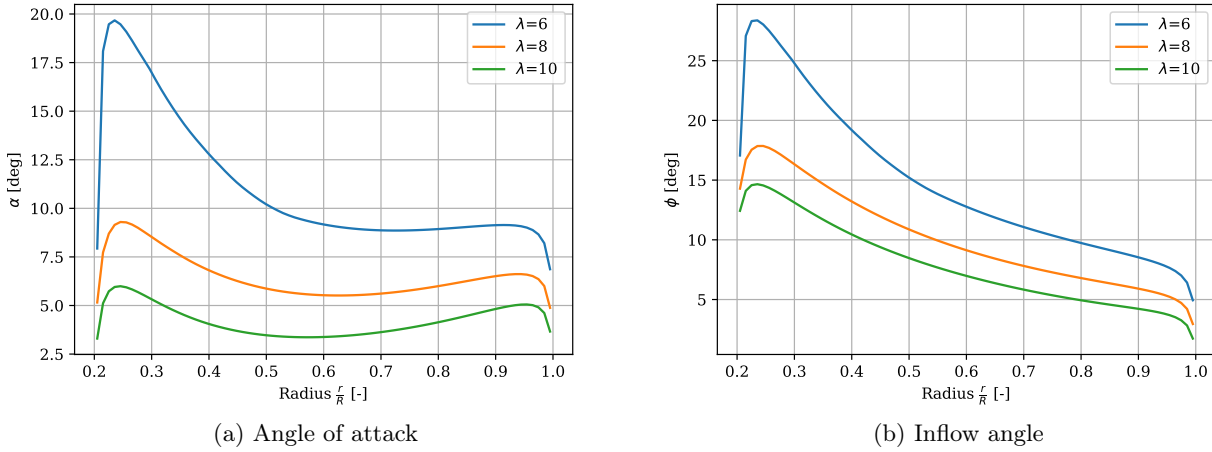(a) Angle of attack   (b) Inflow angle

Figure 8: Radial variation for non yawed rotor with tip speed ratio 6, 8 and 10

Figure 9a shows the change in angle of attack across one blade. It can be observed that the angle of attack generally decreases from tip to root but drops sharply close to the tip and root. A similar behaviour can be seen on Figure 8b with the inflow angle. To explain this, it is best to start from the inflow angle as the angle of attack is a function of the inflow angle.

The inflow angle is dependent on the tangential and normal velocities of the incoming flow as seen in Equation 5. The decreasing inflow angle with radial position can be explained by the fact that tangential velocity increases proportionally to the radius whilst normal velocity remains relatively constant. The behaviour at the root and tip is a result of the Prandtl tip correction on the induction factors. As will be later shown in subsection 6.2, the axial induction factor, a, increases at the root and tip, this decreases the normal velocity and hence decreases the inflow angle. Furthermore, the tangential induction factor a' is only much higher at the root, which increases tangential velocity and further decreases the inflow angle at the root. This explains the larger drop in the value at the root than at the tip.

The angle of attack is defined as the difference between the inflow angle and the blade pitch, which itself is composed of the blade's global pitch and twist as shown in Equation 6. The global pitch is set to $-2°$ and shifts the plot up. The blade twist defines how much the blade is initially angled relative to the flow and in the case of this particular rotor, it decreases linearly from approximately $11°$ at the root to $0°$ at the tip. This therefore explains why the angle of attack distribution is flattened relative to the inflow angle distribution. Closer to the root, there is higher twist and the plot is shifted further down than at the tip where there is no twist.

$$\tan(\phi) = \frac{V_n}{V_t} = \frac{U_\infty(1-a)}{\omega r(1+a')} \qquad (5) \qquad\qquad \alpha = \phi - \theta = \phi - (\theta_g + \beta) \qquad (6)$$

As the incoming wind speed is held constant, varying the TSR will change the rotational speed of the rotor proportionally. Logically, higher TSR and higher rotational speed leads to higher tangential velocity and lower inflow angle and angle of attack. The fact that the angles for a TSR of 6 are so much higher may be due to the axial induction being much lower for this case, leading to higher axial velocity.

𝑇UDelft

6.2 Induction factors

The axial induction factor quantifies the decrease in wind speed created by the presence of the rotor in the flow. As seen on Figure 9a, the axial induction factor is high at the tip and root and somewhat constant in the main blade section. This affect is entirely a result of Prandtl's tip correction factor presented in section 4. To model the effect of a finite number of blades and finite blade length on the actuator disk, the axial induction factor is increased to lower the rotor axial velocity. Outside of the actuator disc, further in the radial direction, the velocity is still the same as the upstream velocity. This means that towards the tip, the amount by which the upstream velocity is reduced by should decrease and velocity should be close to upstream velocity. This is supported by the equation: $a = \frac{U_\infty - U_{rotor}}{U_\infty}$. For increasing TSR, a increases as well. This is logical as in general higher TSR should lead to higher extracted power, meaning higher reduction in upstream velocity and higher axial induction factor. However, this may not be the case for all TSR as passed the optimal TSR, power may start decreasing.

The azimuthal induction factor is highest at the root and goes to zero at the tip. This is to obtain the highest tangential velocity $V_t = \omega R$ at the tip and reduce the tangential velocity at the root to account for the finite number and dimension of blades. There does not seem to be a clear pattern between TSR and a' as all the curves are quite close to one another.
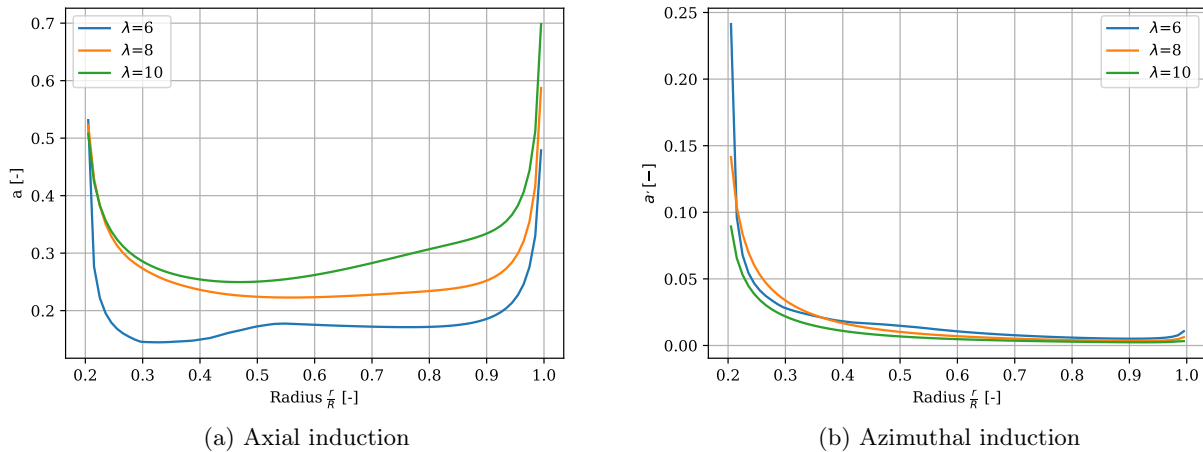

(a) Axial induction

(b) Azimuthal induction

Figure 9: Radial variation for non yawed rotor with tip speed ratio 6, 8 and 10

6.3 Loads

(a) Axial force coefficient
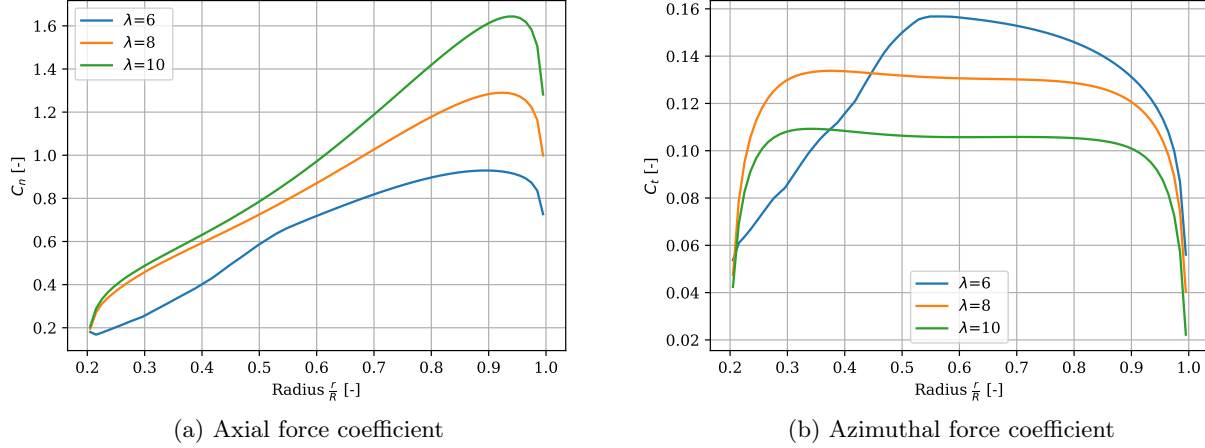
(b) Azimuthal force coefficient

Figure 10: Radial variation for non yawed rotor with tip speed ratio 6, 8 and 10

Figures 10a and 10b give the normalised force coefficients, C_n and C_t, as a function of the normalised radius r/R, for the normal and azimuthal directions, respectively. Normalisation of the thrust and azimuthal loading to these force coefficients facilitates easier comparison with other use cases.

$$C_n = \frac{f_n}{\frac{1}{2}\rho U_\infty^2 c} = C_l(\alpha)\cos\phi + C_d(\alpha)\sin\phi \quad (7) \qquad C_t = \frac{f_t}{\frac{1}{2}\rho U_\infty^2 c} = C_l(\alpha)\sin\phi - C_d(\alpha)\cos\phi \quad (8)$$

Each plot has four features of interest. Firstly there is the general relationship between r/R and the force coefficients. The axial force coefficient, C_n, increases with r/R in a fairly linear fashion, at least for regions unaffected by stall or Prandtl corrections, as will be explained. As shown by Equations 7 and 8, C_n and C_t are both functions of the lift coefficient, drag coefficient, and inflow angle. The difference is in the terms with which the sinusoidal inflow angle terms are associated. For the cases of $\lambda = 8$, and $\lambda = 10$, the range of inflow angles shown in Figure 8b is small, so $\cos\phi > \sin\phi$ and the changes in C_l have a greater effect on C_n than they do on C_t. The decrease in ϕ with r/R observed in Figure 8b, and the fact that C_d is relatively constant over the range of inflow angles (see Figure 2b), lead to the increase in C_n with r/R, whilst C_t does not vary with r/R.

Secondly, there is a relationship between the force coefficients and the tip-speed ratio, λ. This is again due to the effect of tip-speed ratio on the inflow angle. An increase in tip-speed ratio increases the relative magnitude of the azimuthal velocity at the rotor plane, thus decreasing the flow angle as per Equation 5 and Figure 8b. The effect of tip-speed ratio on inflow angle can be seen most clearly in Figure 10a, where as the inflow angle increases with r/R, the difference between the axial force coefficients for $\lambda = 8$ and $\lambda = 10$ is amplified by the $\cos\phi$ term. For the azimuthal force coefficient, this decrease in flow angle with increasing tip-speed ratio increases the size of the $C_d\cos\phi$ term and thus decreases C_t.

Thirdly, the effects of the Prandtl tip and root corrections are evident in both plots. There is a reduction in both axial and azimuthal force coefficients towards the tip and root for all tip-speed ratios except C_n for $\lambda = 6$, which will be attributed to stall in the final observation. Prandtl's correction leads to reductions in both the angle of attack and the flow angle. However, the reduction in angle of attack is steeper than that of the flow angle, and C_l is larger than C_d so both C_n and C_t are reduced.

Finally, the effects of stall are evident in both plots. Between $r/R \approx 0.2$ and $r/R \approx 0.5$ for $\lambda = 6$, the angle of attack exceeds the stall angle of $\approx 10°$ (see Figure 8a). This leads to a reduction in C_l, but, more importantly, a

dramatic increase in C_d. For the axial force coefficient the weighting of the sinusoidal inflow angle terms means these changes lead to a slight reduction in C_n. However, for the azimuthal force coefficient, they cause a more significant reduction.

6.4 Thrust and torque

Table 1: Global power, thrust and torque coefficients with varying TSR

TSR [-]	C_P [-]	C_T [-]	C_Q [-]
6	0.363	0.489	0.0606
8	0.448	0.656	0.0561
10	0.458	0.765	0.0459

Table 1 gives the variation in total thrust coefficient and torque coefficient, C_T and C_Q, with tip-speed ratio. There is an increase in C_T with TSR, which can be attributed to the decrease in inflow angle caused by the increase in ω in the tangential velocity, V_t, in Equation 5. The local thrust coefficient, $C_{T(r)}$, can be related to the axial force coefficient, C_n, as such

$$C_{T(r)} = \frac{B f_{nor} \delta r}{\frac{1}{2}\rho U_\infty^2 2\pi r \delta r} = \frac{\frac{1}{2}\rho U_\infty^2 B c C_n}{\frac{1}{2}\rho U_\infty^2 2\pi r} = C_n \frac{Bc}{2\pi r} = C_n \sigma, \quad \text{where} \quad \sigma = \frac{Bc}{2\pi r}. \tag{9}$$

where f_{nor} is the axial loading on radial element, and σ the solidity of the rotor. It is then clear from Equation 7 and the reasoning in subsection 6.3 that as the inflow angle decreases, C_n, and therefore also $C_{T(r)}$, increases. This increase in the local thrust coefficient can then be related to the increase in global thrust coefficient, C_T, by the integral

$$C_T = \int_{r_{root}}^{R} C_{T(r)} \, dr \tag{10}$$

The decrease in $C_Q(r)$ can also be described by linking it to the azimuthal force coefficient, C_t, as such

$$C_{Q(r)} = \frac{B f_{tan} r \delta r}{\frac{1}{2}\rho U_\infty^2 2\pi r \delta r R} = \frac{\frac{1}{2}\rho U_\infty^2 B c C_t}{\frac{1}{2}\rho U_\infty^2 2\pi R} = C_t \frac{Bc}{2\pi r} \frac{r}{R} = C_t \sigma \frac{r}{R}. \tag{11}$$

Again, applying the logic of subsection 6.3, the decrease in inflow angle now leads to a reduction in C_t, and thus also $C_{Q(r)}$. Again this can be linked to the decrease in the global torque coefficient, C_Q, by the integral

$$C_Q = \int_{r_{root}}^{R} C_{Q(r)} \, dr \tag{12}$$

Finally, the relationship between the global power coefficient and the tip speed ratio can be derived by first addressing the local power coefficient, which can be expressed in terms of the local torque coefficient and the azimuthal force coefficient as such

$$C_{P(r)} = \frac{B f_{tan} \omega r \delta r}{\frac{1}{2}\rho U_\infty^3 2\pi r \delta r} = \frac{\frac{1}{2}\rho U_\infty^2 B c \omega C_t}{\frac{1}{2}\rho U_\infty^3 2\pi} = \frac{Bc}{2\pi r} \frac{\omega r C_t}{U_\infty} = C_t \sigma \frac{\omega r}{U_\infty} = C_{Q(r)} \lambda \tag{13}$$

Again, integrating this over the length of the blade gives the global power coefficient, which can be expressed in temrs of the global torque coefficient.

$$C_P = \int_{r_{root}}^{R} C_{P(r)} \, dr = \lambda \int_{r_{root}}^{R} C_{Q(r)} \, dr = C_Q \lambda \qquad (14)$$

Notably, although C_Q decreases with increasing tip-speed ratio, C_P increases. This can be justified by considering that power is the product of torque and speed. The reduction in C_Q is counteracted by the increase in the non-dimensional speed, the tip speed ratio, in this case. There is a clear levelling off of the increase in C_P within the range of TSRs in question.
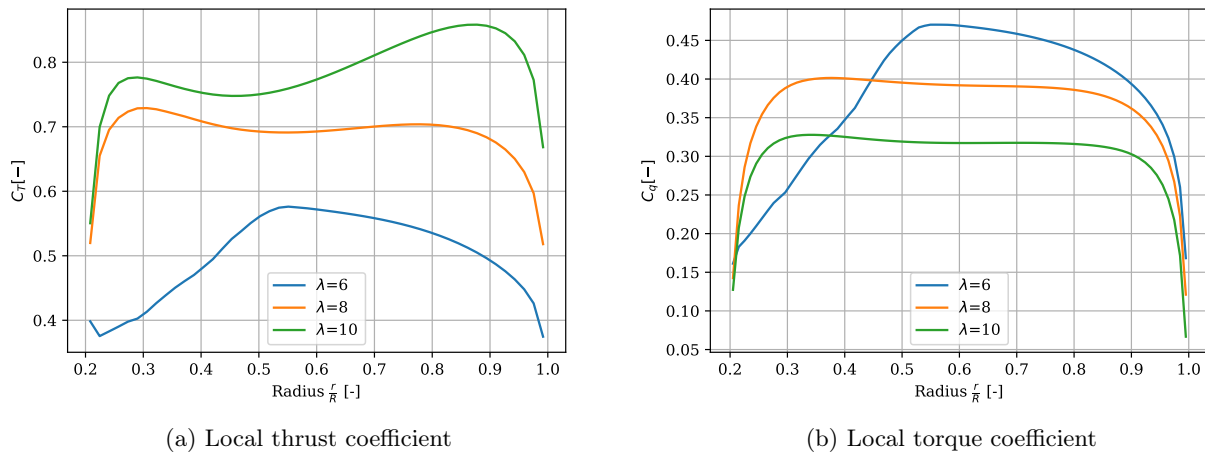

(a) Local thrust coefficient

(b) Local torque coefficient

Figure 11: Radial variation for non-yawed rotor with tip speed ratio 6, 8 and 10.

The relations derived in Equations 9 and 11, can then be used to explain Figures 11a and 11b. The local thrust coefficient simply takes the behaviour of C_n in Figure 10a and removes the dependence on r. The local torque coefficient is almost identical to the azimuthal force coefficient, the only difference being the factor of $Bc/2\pi R$ introduced by in Equation 11.

6.5 Circulation

Figure 12 shows the circulation distribution over the blade. The circulation is dependent on the resulting flow magnitude and direction on the blade as shown by Equation 15. As previously mentioned in subsection 6.1, both normal and tangential velocities are dependent on the induction factors, meanwhile the lift coefficient is dependent on the angle of attack which is also dependent on the velocity direction and induction factors.

When comparing Figure 12 to Figure 9, a clear pattern can be seen especially at the tip and root. At the tip, the flow angle reduces by the effect of the corrected induction coefficients to the extent that the lift coefficient decreases a lot as well, hence leading to a low circulation. Similarly at the root, normal velocity decreases as a increases and tangential velocity decreases not because of a' but because of the radial position ($V_t \propto \omega r$), resulting in both a low flow angle and low relative velocity, which leads to a lower circulation at the root as well. In the centre of the blade, the variation in circulation is also mainly as a result of the changes in a. Vorticity can be obtained by taking the gradient of the circulation. As a result of the changes in circulation along the blade the blade sheds vorticity sheets as it rotates. Furthermore, larger gradients of circulation are seen at the tip and root, meaning more vorticity is shed by the tip and root vortices compared to the centre of the blade.

The noticeable difference between the circulation variations at different TSR is the different shape for a TSR of 6. This is due to the high angle of attacks observed in Figure 8a at radial positions 0.2 to 0.5 which leads to lower values of the lift coefficient (see Figure 2a).

$$\Gamma = \frac{1}{2}VC_lc = \frac{1}{2}\sqrt{V_t^2 + V_n^2}C_lc \tag{15}$$
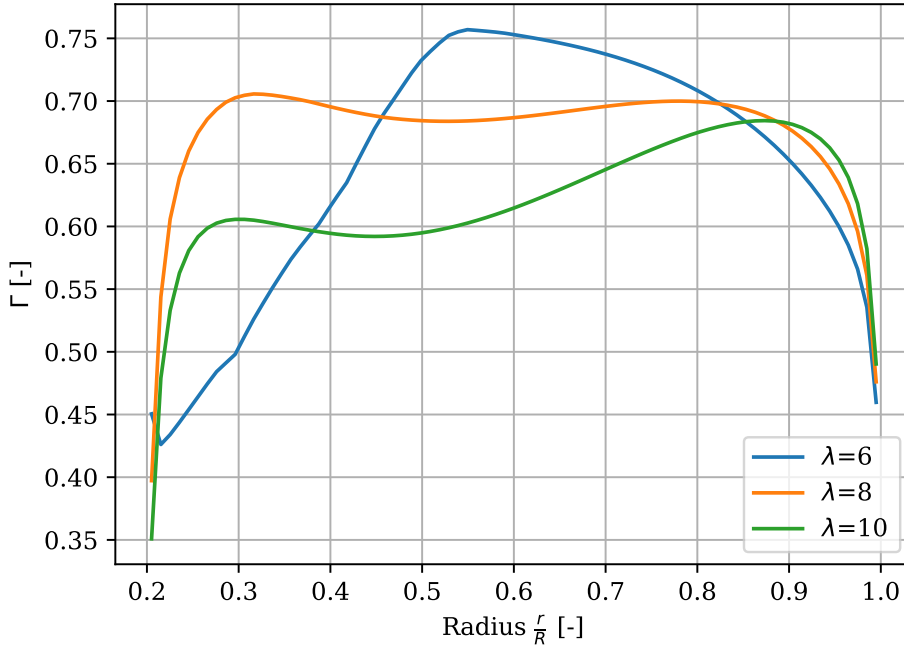

Figure 12: Circulation radial variation for non-yawed rotor with tip speed ratio 6, 8 and 10.

6.6 Stagnation enthalpy

Figure 13 presents the change in stagnation enthalpy in the stream tube that passes through the rotor. The stagnation enthalpy is measured in energy per unit mass and represents the energy required to bring the flow isotropically to a stagnation point or at rest. Note that for simplicity, the internal energy of the flow has been omitted. As the magnitude of the upstream pressure $p_\infty = 101325$Pa is quite large relative to the changes in dynamic pressure introduced by the changes in velocity, p_∞ was set to 0 to better represent the variations in enthalpy. Furthermore, the scale shown on Figure 13 is only relevant for the discs in the downwind position to capture more of the variation in enthalpy across the discs.

Due to the presence of the rotor in the flow, the flow is deflected and expands approaching the rotor which according to the continuity equation reduced velocity. The fraction of representing the reduction in free stream velocity at the rotor is the axial induction factor. For an upwind infinity velocity of U_∞, the velocity at the rotor (both upwind and downwind of rotor) is defined by Equation 17 and the velocity at infinity downstream by Equation 18. As seen from Equation 16, enthalpy varies with pressure and velocity. From upwind infinity to in front of the rotor, pressure increases and velocity decreases, this causes an expansion of the streamlines of the flow. However as energy is yet to be extracted from the flow, the enthalpy does not change. Across the rotor surface, a pressure drop occurs and causes a drop in enthalpy. As see on the third disc in Figure 13, more energy is extracted in the centre of the blade compared to the tip and root of the blade as enthalpy values remain higher there. This is due to the formation of tip vortices on the finite blade, reducing loads. From right after the rotor to infinity downwind, no more energy is extracted. The static pressure increases and returns to its initial value of p_∞ and the dynamic pressure and hence velocity decrease. This causes a further expansion

of the streamlines. The radial distribution of enthalpy is similar to the one at the rotor downwind position but spread over a larger radius.

$$h_0 = \frac{p_\infty}{\rho} + \frac{1}{2}V_\infty^2 - \Delta p \qquad (16)$$

$$U_{rotor} = U_\infty(1-a) \qquad (17)$$
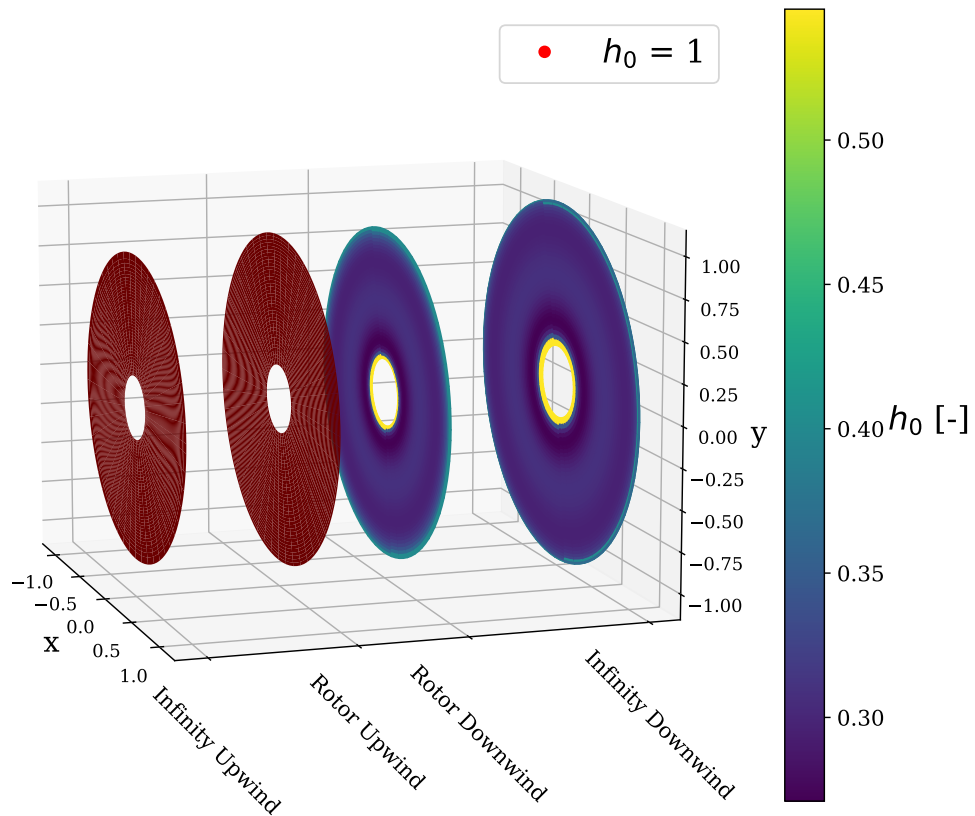
$$U_{downwind} = U_\infty(1-2a) \qquad (18)$$

Figure 13: Change in stagnation enthalpy from infinity upstream to infinity downstream through non-yawed rotor at $\lambda = 8$. Values are normalised relative to the infinity upwind enthalpy.

7 Yawed Rotor Results

In this section, the results of the BEM code for three yaw angles: 0, 15 and 30 degrees are compared for various parameters at a TSR of 8. It is important to note that the plots show the vertical plane of the rotor, with the rotor rotating clockwise, viewed from the front as shown in Figure 14. From the blade's point of view, the flow is therefore flowing in a counterclockwise direction. The yaw angle is defined as counterclockwise positive from the central axis in the horizontal plane.
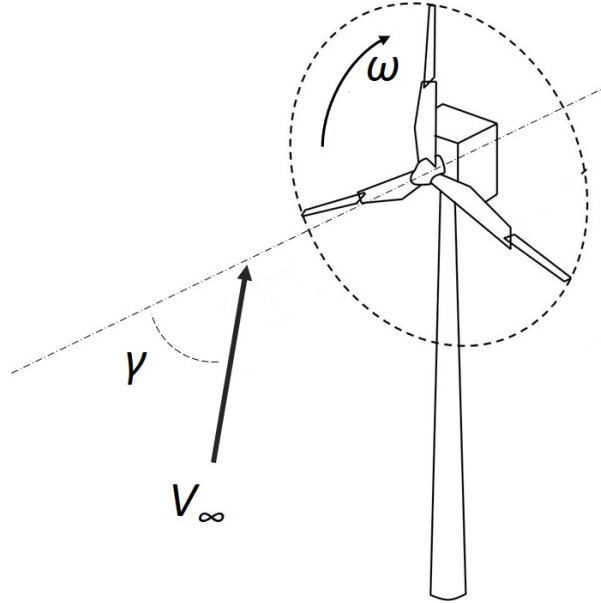
Figure 14: Yaw angle reference frame

7.1 Angle of attack and inflow angle

Figure 15 and Figure 16 show the radial and azimuthal variations of the angle of attack and inflow angle, respectively. Similarly to the non-yawed case, the angle of attack depends and inflow angle both show similar behaviour as the former depends on the latter. The reasoning presented in subsection 6.1 is still applicable to the yawed case as along the radius, yaw will affect the magnitude of values. The shape of the the radial variations should therefore remain relatively close to the ones in a non-yawed case.

The velocities are now a function of yaw angle γ as shown in Equation 19. The normal component of velocity only varies in magnitude and does not introduce azimuthal changes. This effect can be seen from in central part of the blade (radial positions 0.4 to 0.8), where as yaw increases, the magnitude of the two angles decreases. The tangential velocity however varies depending on the azimuthal position. From both of the polar plots shown below, it can seen that the top side shows lower values than the bottom side, this is due to the fact that tangential velocity is larger at the top. For azimuthal positions of 0° to 180°, the sin function is positive, meaning that the flow due to yaw is in the same direction as the tangential velocity due to the turbine rotation. This is the opposite on the lower half plane, where the incoming wind is in the opposite direction (negative sin function) to the rotor tangential velocity. The resulting tangential component experienced by the blade is therefore lower, leading to higher values of inflow angle and angle of attack at the bottom.

$$\tan(\phi) = \frac{V_n}{V_t} = \frac{U_\infty(\cos\gamma - a)}{\omega r(1 + a') + U_\infty \sin\gamma \sin\Psi} \tag{19}$$
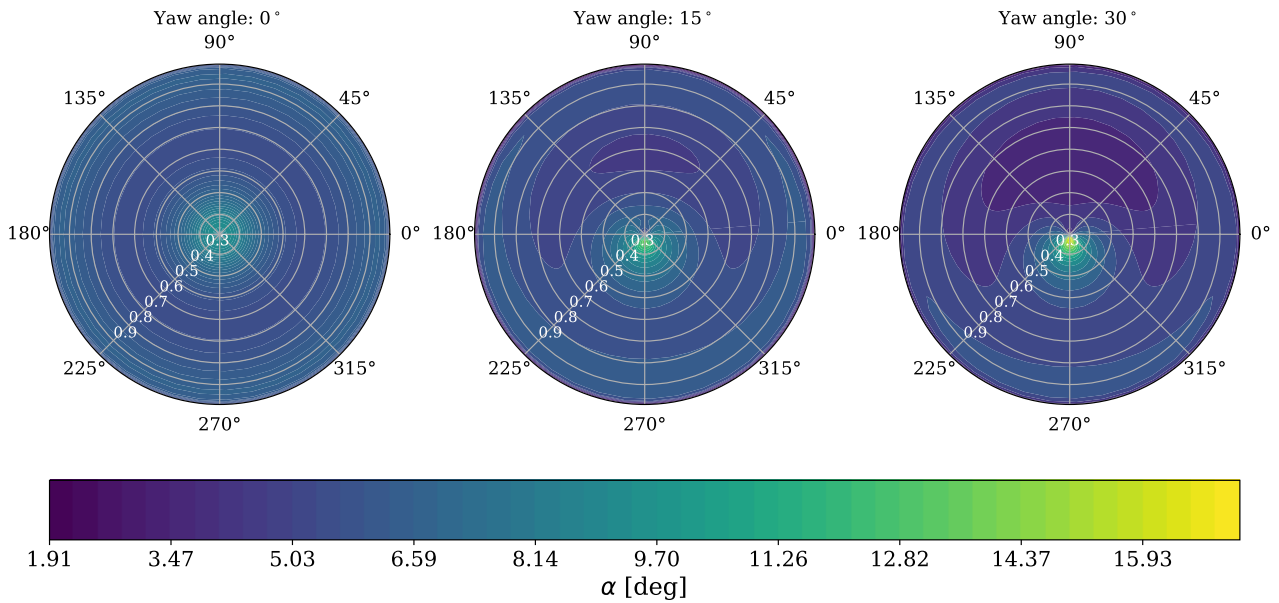
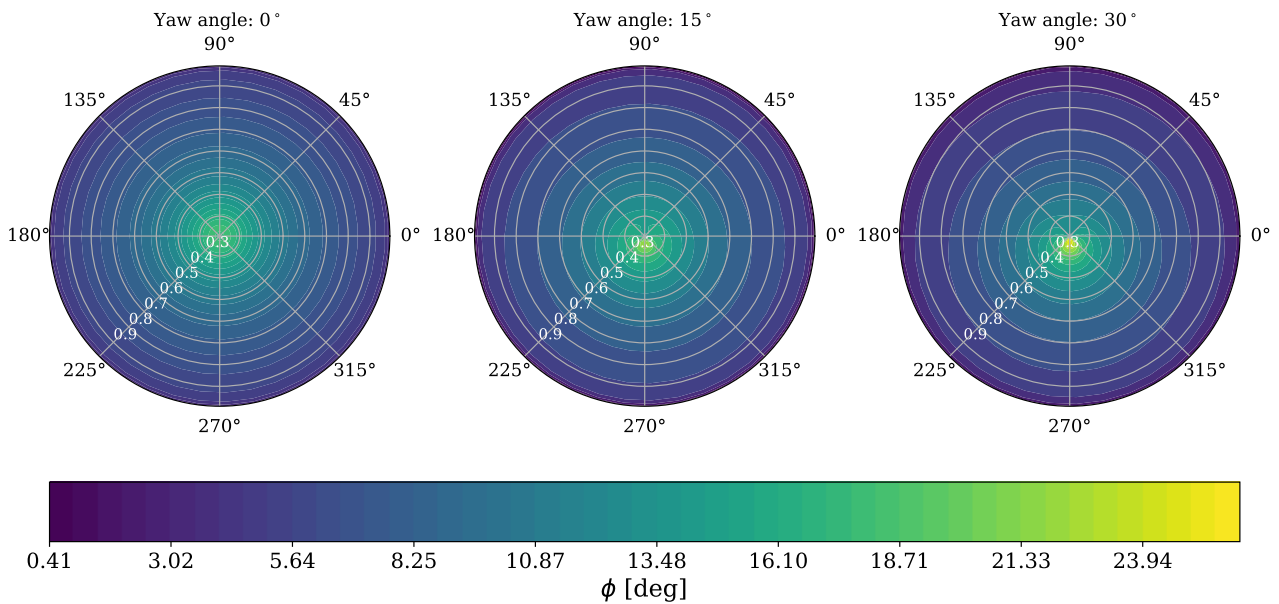Figure 15: Angle of attack polar plots for yaw angles 0°, 15°and 30°

Figure 16: Inflow angle polar plots for yaw angles 0°, 15°and 30°

7.2 Induction factors

Figure 17 and Figure 18 show the changes in axial and azimuthal induction factors when the turbine is exposed to velocity at a yaw angle. As the induction factors reach high values close to the tip and root, it is difficult to effectively capture much variation on the rest of the blade. Therefore, the scale of both plots as been adjusted in order see more changes azimuthally and radially.

The same pattern as for the inflow and angle of attack is seen on the induction factors for yaw cases. In general, the magnitude of the axial induction decreases with increasing yaw angle as less energy can now be extracted as the rotor experiences an axial velocity corrected by the cosine of the yaw angle. There is also clear split between the top half and bottom half of the actuator disc. This is due to the fact that in the upper half (0°to 180°), there is an increase in tangential velocity over the blade. More energy is therefore available compared to the lower half where lower tangential velocities occur and less energy can be extracted. The azimuthal induction factor appears to slightly decrease in magnitude with increasing yaw angle. As the magnitude of a' is already small, the variations are also therefore quite small. It can be noticed that near the root and in the lower half, the values of a' tend to be lower for higher yaw angles.

For a yaw angle of 15° it is quite surprising to see an increase in a at the tip relative to the non-yawed case. This turned out to be a greater issue for lower yaw angles and in particular with the Glauert correction of yawed cases giving too high values.
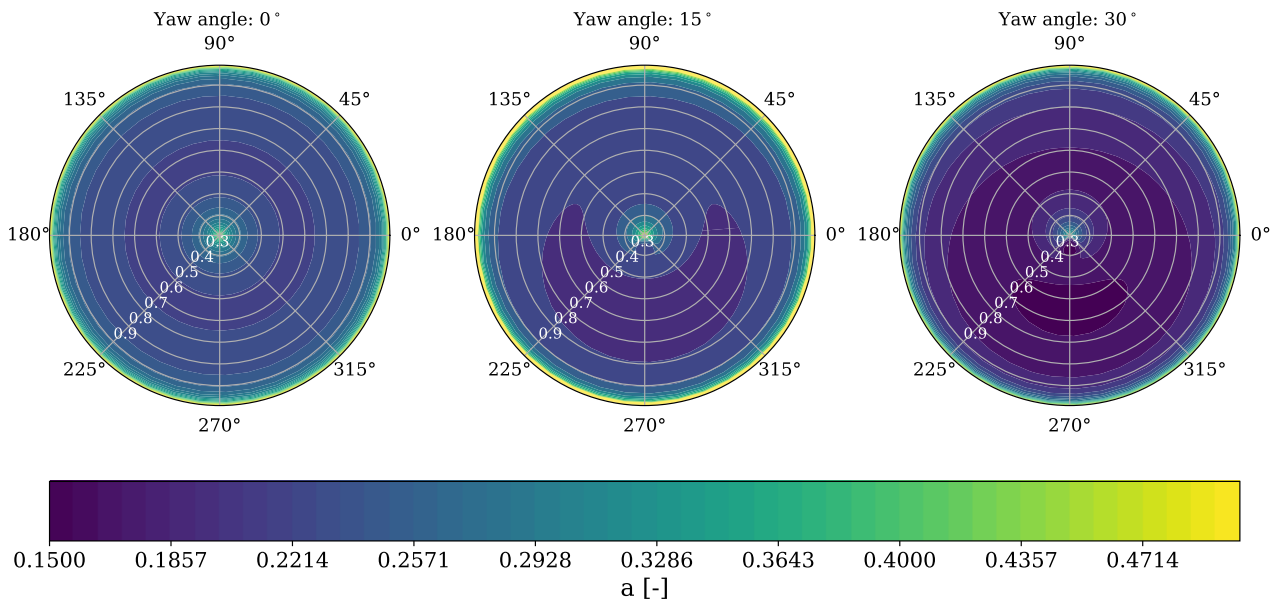

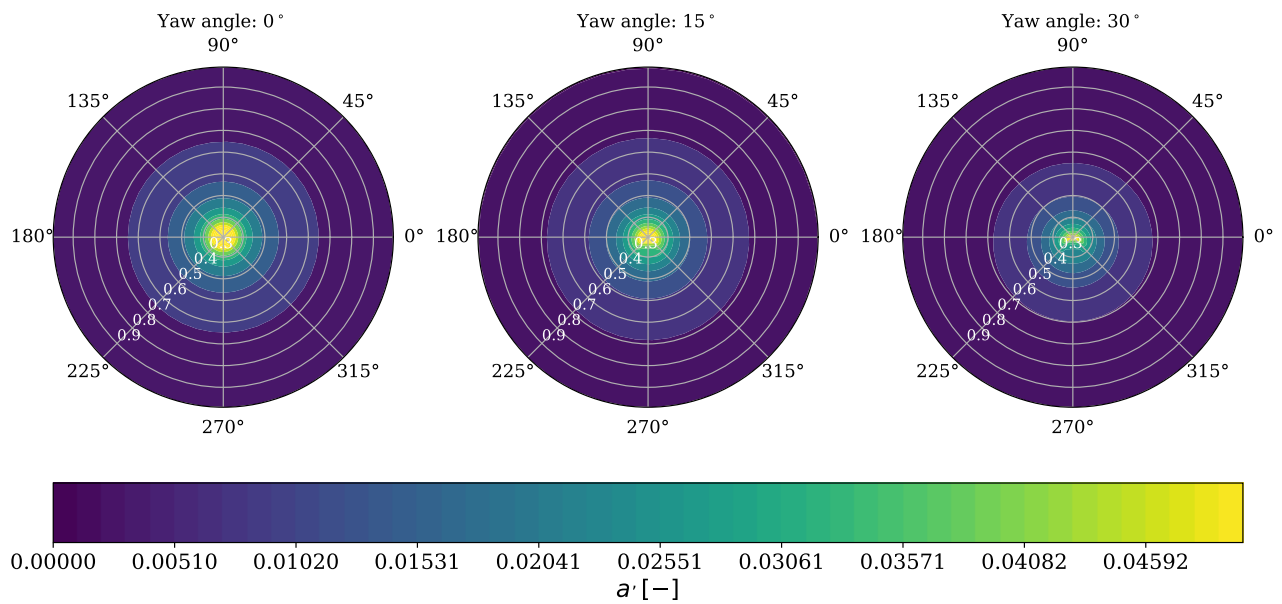Figure 17: Axial induction polar plots for yaw angles 0°, 15°and 30°

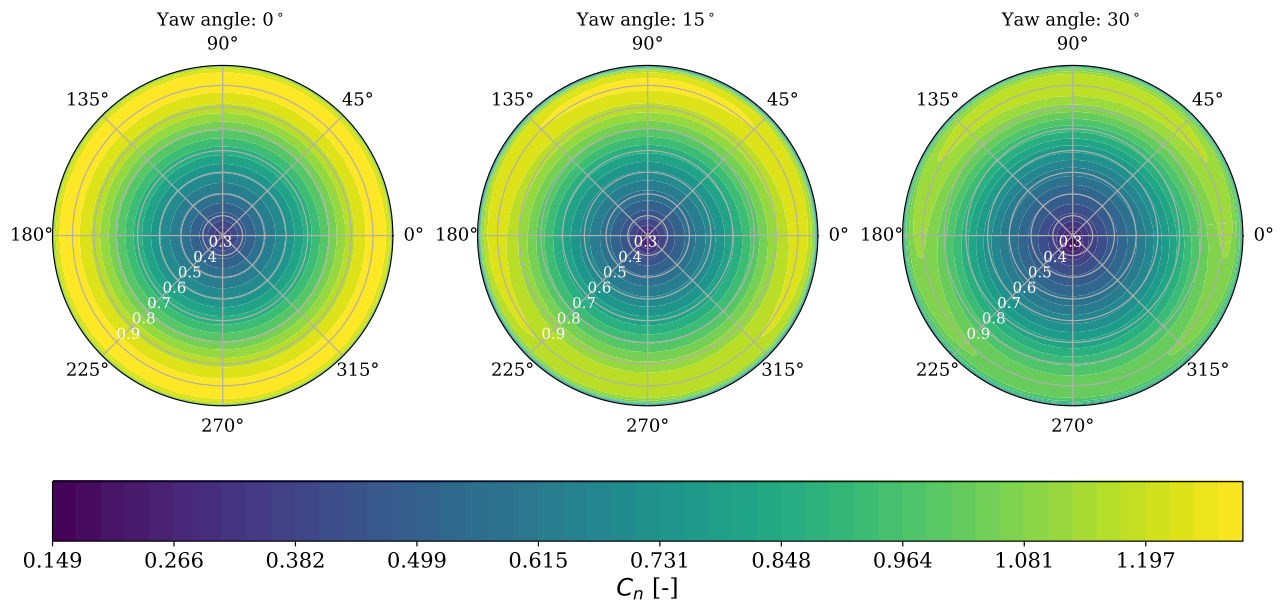Figure 18: Azimuthal induction polar plots for yaw angles 0°, 15°and 30°

7.3 Loads

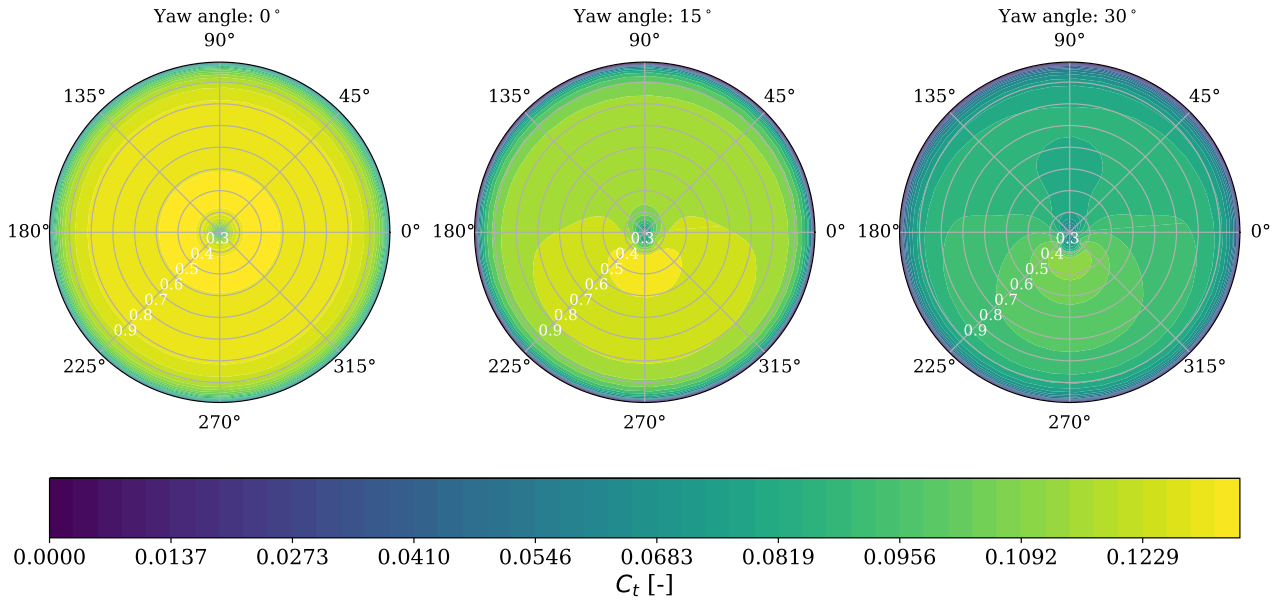Figure 19: Axial force coefficient polar plots for yaw angles 0°, 15°and 30°

Figure 20: Azimuthal force coefficient polar plots for yaw angles 0°, 15°and 30°

Figures 19 and 20 show the radial and azimuthal variations of the axial and tangential force coefficients, respectively. For the axial force coefficient, the relevant features described in subsection 6.3, i.e. the increase of C_n with r/R and the effects of the Prandtl tip and root corrections, still apply. However, there are now two additional features, namely the reduction of C_n and the asymmetries about the horizontal that arise with increasing yaw angle. As mentioned in sections 7.1 and 7.2, the yaw angle leads to a reduction in the axial velocity, which reduces the angle of attack, the lift coefficient, and therefore the axial force coefficient. The sinusoidal variation of the azimuthal velocity component, V_t, also creates an azimuthal variation in inflow angle, which is reflected in the azimuthal variation of C_n. Where inflow angle is lowest, at $\Psi = 270°$, C_n is also a minimum. This is most evident near $r/R \approx 0.9$, where the azimuthal variation of C_n is clearest.

Similar to the non-yawed case, the azimuthal force coefficient shows much less variation with r/R, apart from the tip and root loss regions. C_t also reduces with increasing yaw angle and exhibits asymmtery about the horizontal. Again, C_t shows the opposite behaviour with respect to the inflow angle, i.e. where ϕ is minimum at $\Psi = 270°$, C_t is largest.

7.4   Thrust and torque

Table 2: Global thrust and torque coefficients with varying yaw angle

Yaw angle [°]	C_P [-]	C_T [-]	C_Q [-]
0	0.448	0.656	0.0561
15	0.395	0.616	0.0495
30	0.303	0.546	0.0379

Table 2 gives the variation of total thrust coefficient, C_T, and total torque coefficient, C_Q, with yaw angle. There is a decrease in C_T with yaw angle, which can be attributed to the general decrease in C_n described in the previous section and the relationship given in Equation 9. Likewise, the reduction in C_Q can be linked to

the reduction in C_t shown in Figure 20 and the relationship given in Equation 11. Equation 14 then links this to the decrease in C_P, given the tip-speed ratio remains constant.

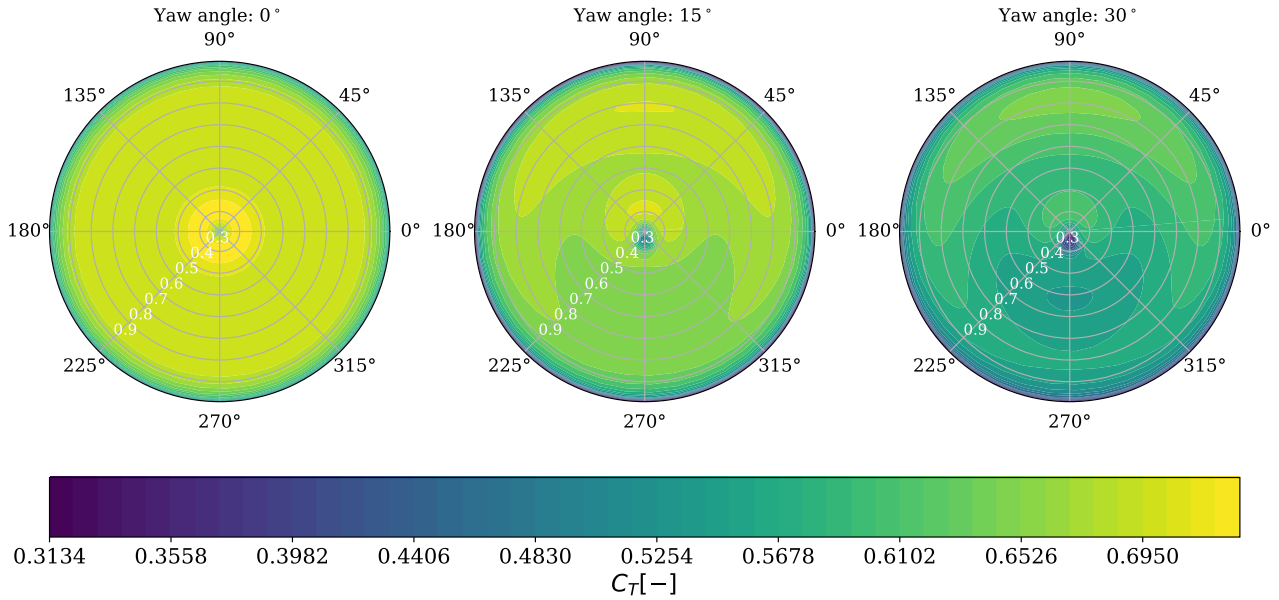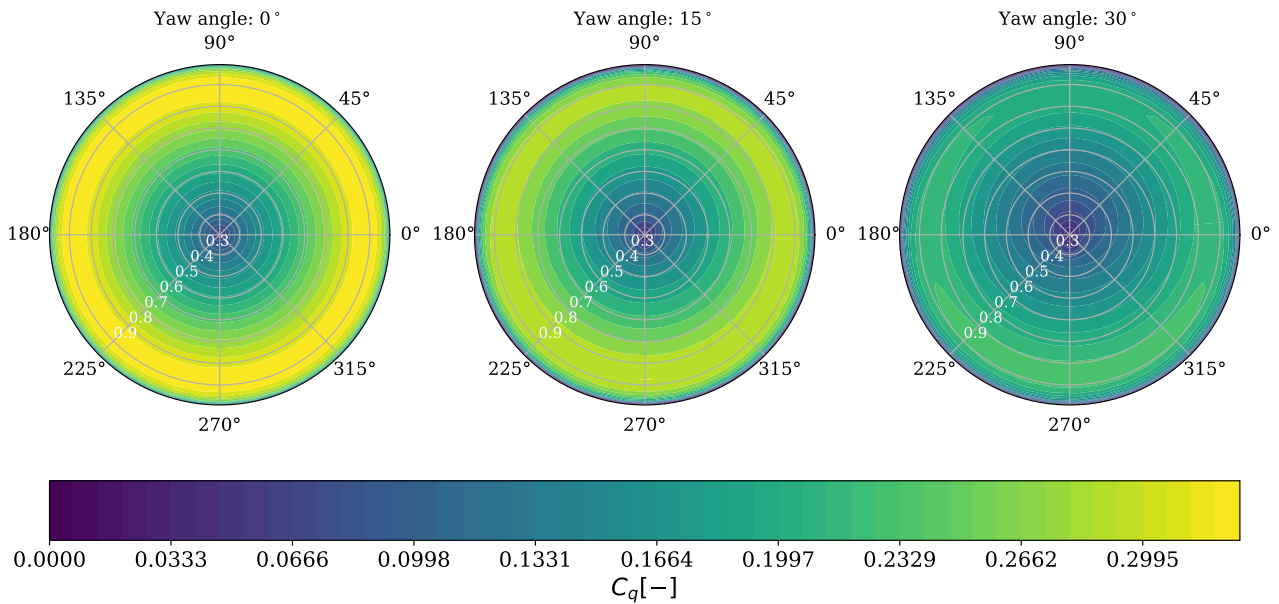Figure 21: Local thrust polar plots for yaw angles 0°, 15°and 30°

Figure 22: Local torque polar plots for yaw angles 0°, 15°and 30°

The same equations (9 and 11) can be used to explain the behaviours shown in Figures 21 and 22. The scale of Figure 21 means that it provides the clearest picture of the behaviour of any of these plots. Again there is an asymmetry about the horizontal, and the isosurfaces also show the radial variation for the yawed case well.

22

7.5   Circulation

Figure 23 presents the circulation as a function of radial and azimuthal positions. As expected, the value of circulation generally decreases with increasing yaw due to the decrease in axial velocity the rotor disc experiences. Once again, higher values are found in the upper half of the disc as in this region, the tangential component of the yawed wind speed is in the same direction as the tangential velocity due to the turbine's rotation. Higher tangential velocity leads to higher circulation as seen by Equation 15. As explained in subsection 6.5, the gradient of circulation represents the vorticity. Radial variations in circulation can still be seen and vorticity is still shed along the blade. As azimuthal variations in circulation are now present, gradients occur in azimuthal direction and vorticity is also shed in that direction. The vortex wake will therefore be shifted in the same direction as the incoming yawed velocity.
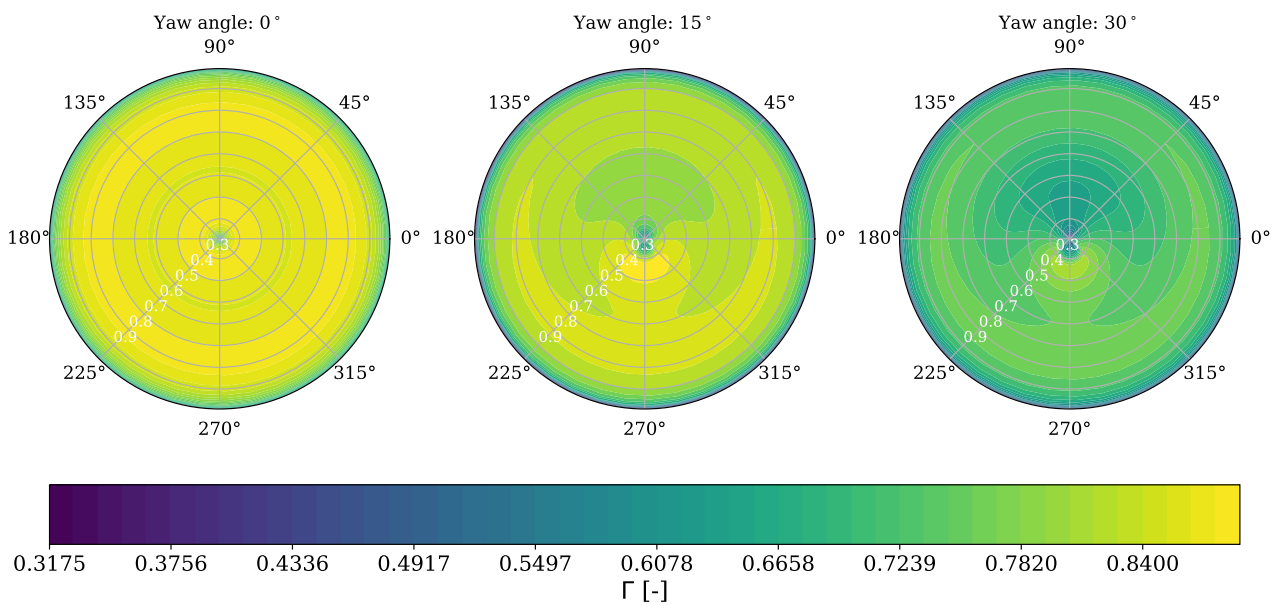

Figure 23: Circulation polar plots for yaw angles 0°, 15°and 30°

8 Optimisation Results

In this section the results for the re-design, or optimisation, will be presented. Firstly, the design procedure will be explained. Then, the blade geometry obtained will be presented, and its performance will be compared to the original design. The design objective is to fix the thrust coefficient at 0.75 while maximising the power, for a tip speed ratio of $\lambda = 8$. The blade radius and airfoil used are kept unchanged.

8.1 Design procedure used

The design procedure used follows the method described by Christian Back in *Aerodynamic Design of Wind Turbine Rotors* [15] and during the course "Loads, Aerodynamics, and Control of Wind Turbines" taught at DTU. The method allows a blade design with different airfoils and a varying relative thickness, but this has not been used as the blade has only a single airfoil. The main idea is to select a design axial induction factor and the desired operational point of the airfoil, and solve for each radius the BEMT equations, taking the chord $c(r)$ and the tangential induction factor $a'(r)$ as the design output.

The BEMT equations can be solved in terms of these two parameters, leading:

$$c = \frac{a}{1-a} \frac{4F\sin^2\phi}{C_n} 2\pi r \qquad (20)$$

$$a' = \frac{1}{\dfrac{4F\sin\phi\cos\phi}{\sigma C_t} - 1} \qquad (21)$$

These two equations are solved using least squares method after computing the necessary preceding equations (flow angle, Prandtl losses, force coefficients, and solidity). This method includes a root and tip correction, and therefore the geometry will try to adapt to it. The mathematical solution makes the chord tend to zero at the tip and the root. In order to have a finite and realistic value, the minim chord values have been bounded. The minimum value at the tip is set to 0.3m, and at the root, 1.5m.

These external constraints imply that the desired axial induction factor a will not be matched in the reality. Therefore, an iterative procedure should be established to ensure that the design a is matched (and, eventually, the design C_T). The value of a for the first design is estimated using the optimal Glauert equation, and the subsequent a are corrected taking into account the actual axial induction factor resulting from the design. A flowchart of the procedure used is presented below:
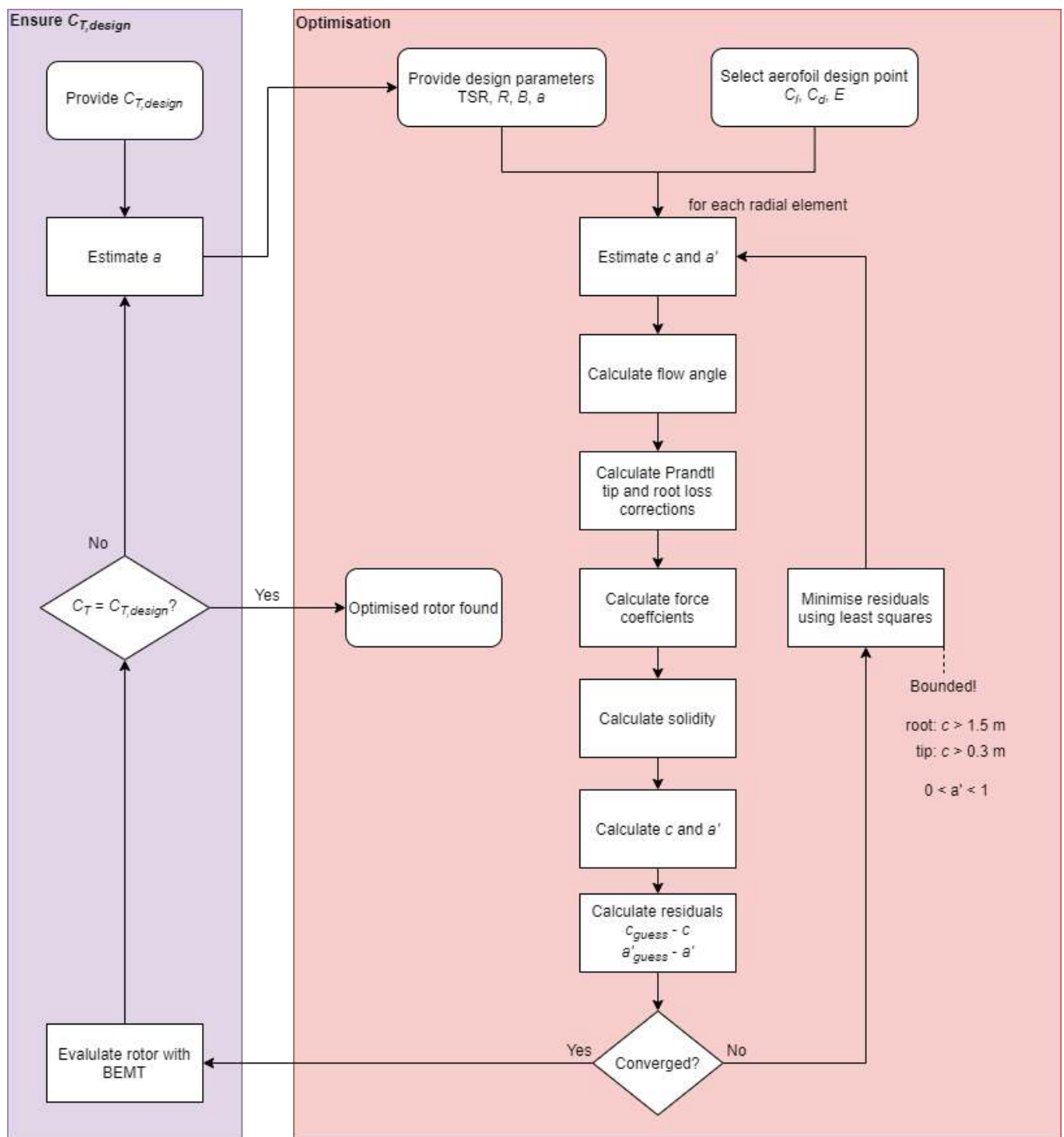
Figure 24: Flowchart for optimisation code.

8.2 Design obtained and comparison with the original blade planform

The design obtained will be presented and compared to the original blade in this section.

(a) Comparison of chord distributions.
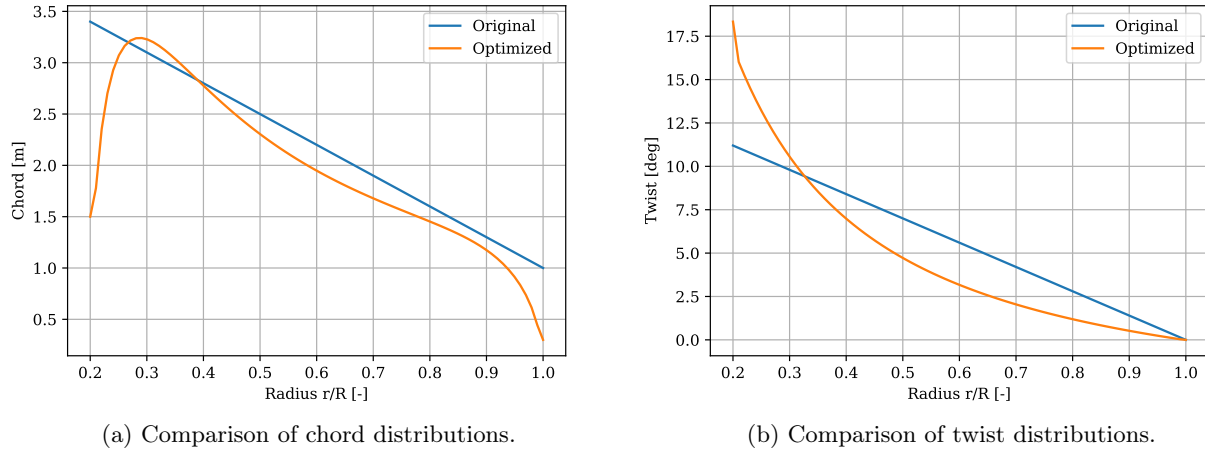
(b) Comparison of twist distributions.

Figure 25: Twist and chord distribution for the original and the new design.

The chord has a similar shape as the original blade, but it tries to correct the root and tip losses by setting a lower chord. As the minimum values are bounded, it does not go to zero, which is the mathematical solution as $F \to 0$. The twist has been selected such that the angle of attack seen by the blade at each section is the design value selected $(\beta(r) = \phi(r) - \alpha_{des})$. It is also imposed that the twist at the tip should be zero, which gives the design pitch angle θ.

The two blade geometries have been compared using the classic $C_P = f(\lambda, \theta)$ contour plots. The plots are presented below:

(a) Original design.

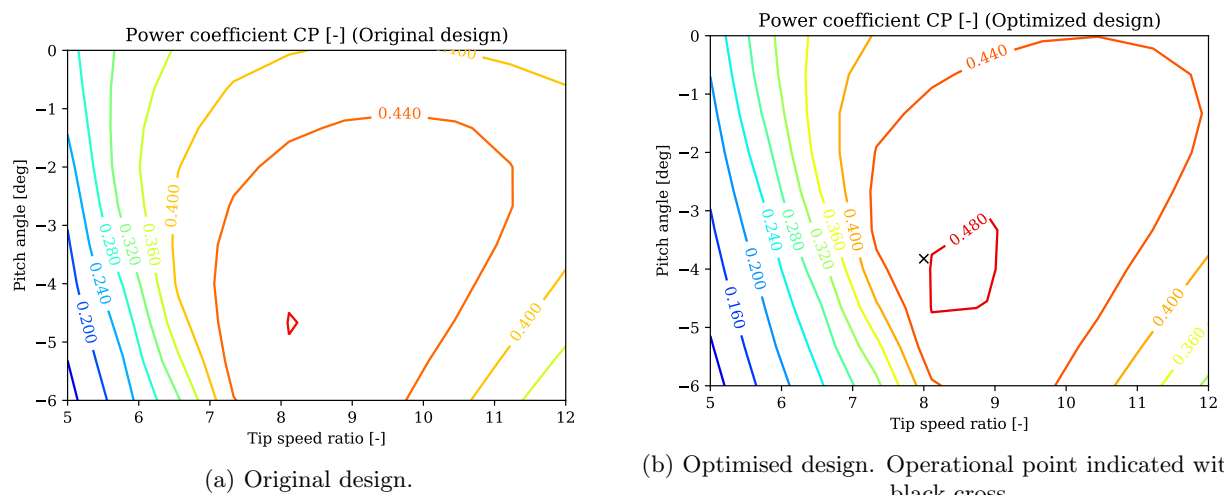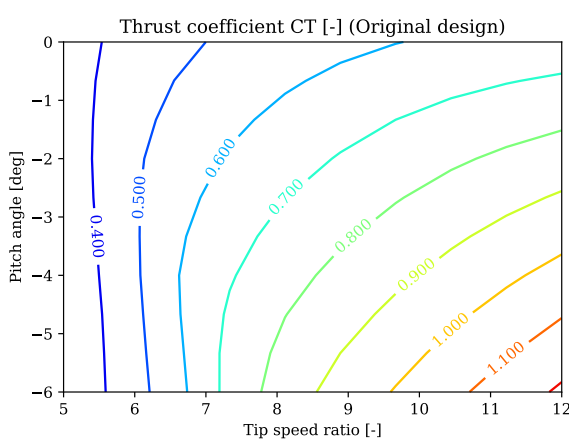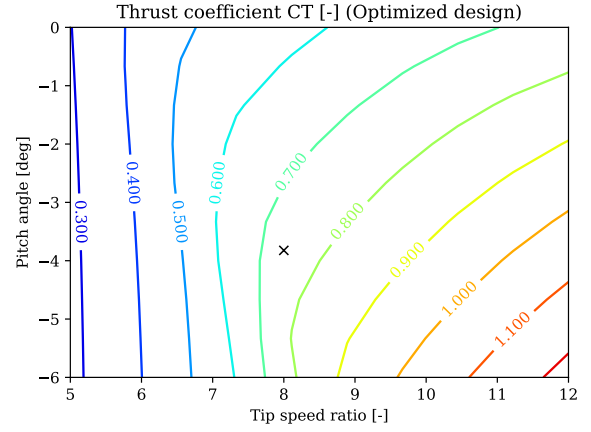(b) Optimised design. Operational point indicated with a black cross.

Figure 26: Pitch-tip speed ratio-CP contour plots for the original and the new design.

An increase of C_P has been reached: 0.479 from the 4.448 of the original design (at $\lambda = 8$ and taking into

account $\theta_{org} = -2$). Moreover, there is a significant room for improvement by operating in a higher TSR. Nonetheless, maximising the power coefficient was only one of the two objectives of the design, the other being prescribe the thrust coefficient at 0.75. If it was desired to increase the power coefficient, the thrust coefficient would also increase. This may be seen in the contour plots for C_T:
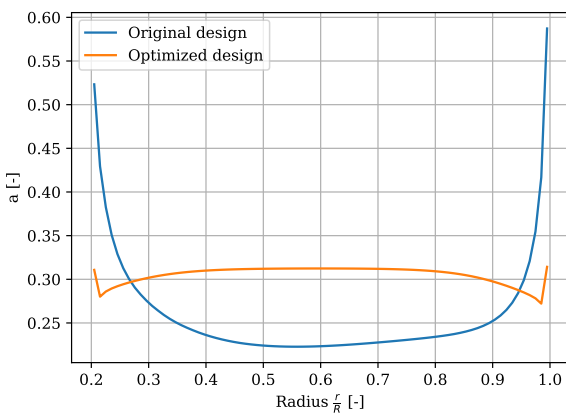

(a) Original design.

(b) Optimised design. Operational point indicated with a black cross.

Figure 27: Pitch-tip speed ratio-CT contour plots for the original and the new design.

Very similar results are obtained in this plot. The main takeaway is that in order to increase C_P as discussed before, the desired C_T would no longer be obtained. This is consistent with the optimal $C_P, C_T = f(a)$ curves, where the maximum C_P is obtained at $C_T = 8/9 > 0.75$. The effect of the Glauert correction for heavily loaded rotors is present here: the maximum C_P is not obtained at the same location as the maximum C_P as observed in the ideal case. Instead, one can keep on increasing C_T while C_P decreases for the region $a > 0.3$.

The following plots show a comparison of the main BEMT variables over the span of both blades. They have been analysed at $\lambda = 8$ and no yaw misalignment.

(a) Axial induction factor.
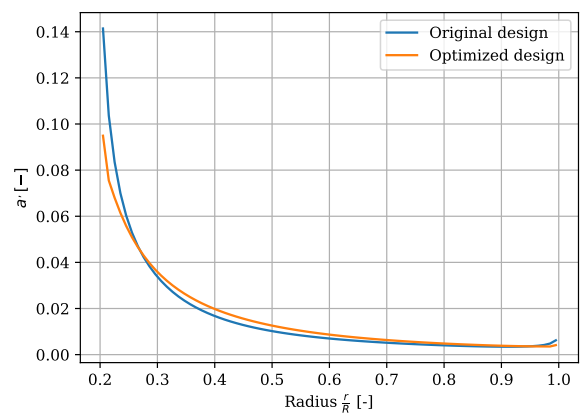
(b) Tangential induction factor.

Figure 28: Induction factors as a function of radius for the original and the new design.

The goal of the design procedure was to get a constant axial induction factor distribution. The results are satisfactory, because little variation is observed in the optimised case. The effects of prescribing the minimum chord can be clearly seen in the tip and the root. The value of induction is also closer to the optimal $a = 1/3$, which explains the higher power coefficient of the new design.
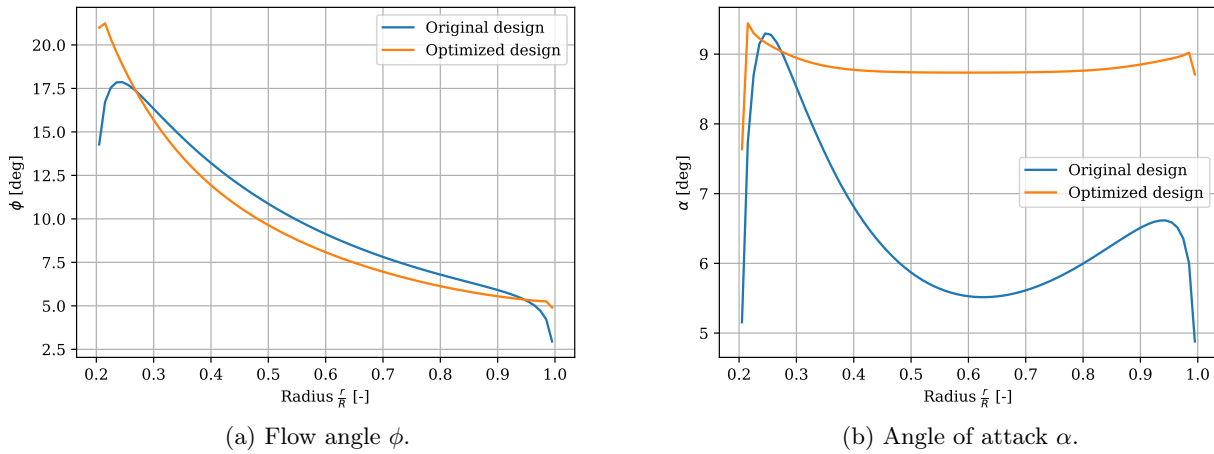

(a) Flow angle ϕ.

(b) Angle of attack α.

Figure 29: Flow angle and angle of attack as a function of radius for the original and the new design.

The flow angle ϕ is very similar, because the operational conditions are the same. The only variations are given by the different values of the induction factors. However, the angle of attack α is different between both rotors, and it is clear the design objective for this parameter: to be as close as possible to the design angle of attack α_{des}. Ideally, it would be desired to operate at this point throughout all the blade span, because it is the E_{max} point of the airfoil that minimises the viscous losses of the blade.
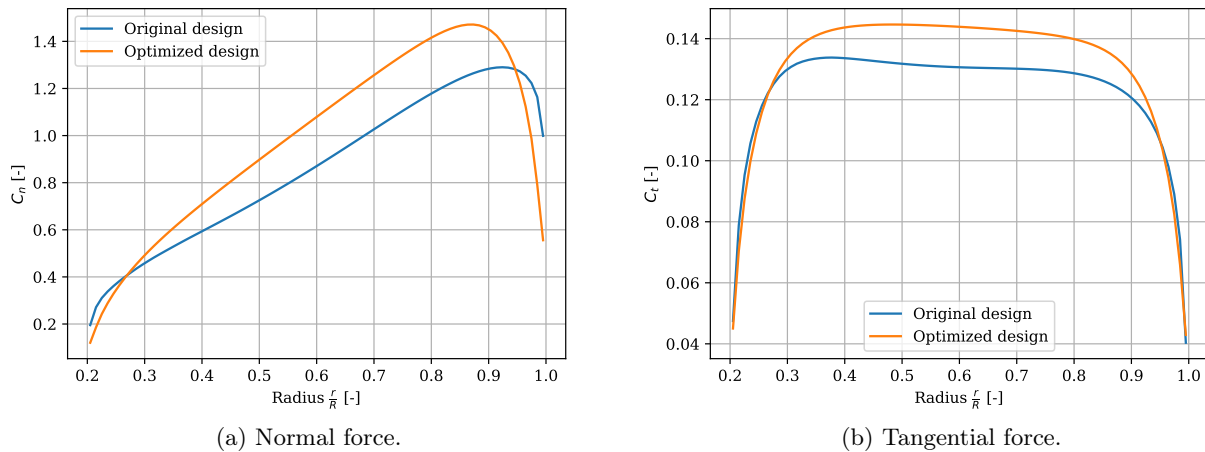

(a) Normal force.

(b) Tangential force.

Figure 30: Normal and tangential force coefficients as a function of radius for the original and the new design.

The consequence of the different operational point of the airfoil is observed looking at the force coefficient. At $\mu \approx 0.25$, where the angle of attack was very similar for both designs, the force coefficient matches. However,

in the outer section of the blade, where α is higher for the new design, a higher C_l is obtained as well, which is translated into both the normal and the tangential force coefficients.
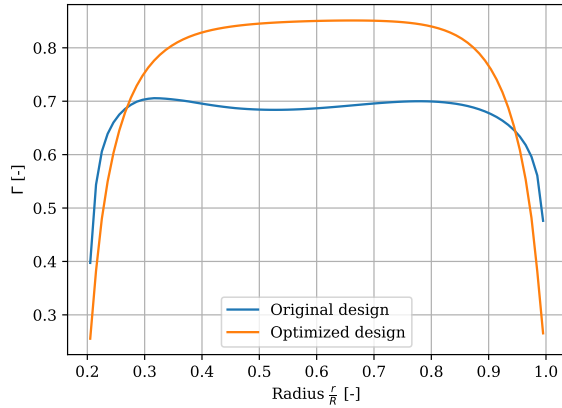
(a) Circulation.
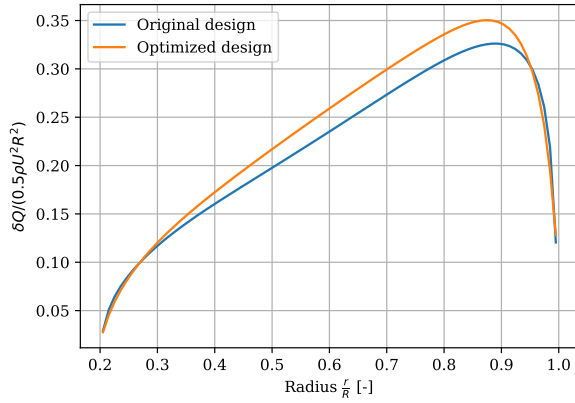
(b) Torque coefficient.

Figure 31: Circulation and torque coefficient as a function of radius for the original and the new design.

Finally, the better performance may also be analysed from the perspective of the circulation. The higher lift aforementioned generates more vorticity in most of the blade, which increases the circulation strength. It is also interesting to look at the torque contribution for each section (non-dimensionalised by qR^2). The new design clearly produces more torque in the important region: the outer sections excluding the very tip.

9 Conclusion

For the original blade design, performance has been compared for a range of tip-speed ratios. This includes analysis of angle of attack and inflow angle, induction factors, loads, total thrust and torque, circulation and stagnation enthalpy. Looking at performance from the perspective of thrust, power and torque coefficients the following conclusions can be drawn:

- Increasing tip-speed ratios increases global thrust coefficient. This is due to the reduction in tip losses. However, there will come a point where the increase in tip-speed ratio reduces the inflow angle to an extent that the viscous forces created by the drag force outweigh the reduction in tip losses.

- Increasing tip-speed ratios decreases global torque coefficient. This is due to the decrease in the azimuthal force coefficient.

- Increasing tip-speed ratio increases global power coefficient within the range of tip-speed ratios investigated. However, there is clearly a levelling off, and the expectation is that this would reach a maximum, given the tradeoff between increasing speed and decreasing torque.

Following this, the performance of the original design was then compared for three rotor yaw angles at a single tip speed ratio, the same parameters were investigated as for the non-yawed case, and the following conclusions can be derived regarding the performance under yaw

- Increasing yaw reduces thrust coefficient, because increasing yaw reduces the magnitude of the axial velocity, and has no azimuthally averaged contribution to the tangential velocity, thus the magnitude of the relative velocity is reduced. This reduction in relative velocity reduces the magnitude of lift, thus the loading and so the thrust.

- Increasing yaw reduces power coefficient. The same argument applies as for thrust, except now the reduction in the azimuthal force coefficient causes the reduction in C_P.

- Increasing yaw reduces torque coefficient. Again due to the decrease in the azimuthal force coefficient.

Effects of optimisation: Using the method described by C. Bak [15], a new blade geometry has been designed for a $C_T = 0.75$ while maximising C_P.

- A power coefficient increase has been obtained compared to the original geometry (0.479 from 0.448).

- The new operation is more consistent: less variation of a and α.

- There is still room for a higher C_P, but a higher C_T would be required to achieve so.

References

[1] J. Ledoux, S. Riffo, J. Salomon *et al.*, "Analysis of the Blade Element Momentum Theory," *arXiv preprint arXiv:2004.11100*, 2020.

[2] W. Froude, "On the elementary relation between pitch, slip, and propulsive efficiency," *Transactions of the Royal Institution of Naval Architects*, vol. 19, pp. 22–33, 1878.

[3] W. J. M. Rankine, "On the mechanical principles of the action of propellers," *Transactions of the Institution of Naval Architects*, vol. 6, 1865.

[4] F. W. Lanchester, "A contribution to the theory of propulsion and the screw propeller," *Journal of the American Society for Naval Engineers*, vol. 27, no. 2, pp. 509–510, 1915.

[5] A. Betz, "Das Maximum der theoretisch möglichen Ausnutzung des Windes durch Windmotoren," *Zeitschrift fur das gesamte Turbinenwesten*, vol. 20, 1920.

[6] N. Joukowsky, "Windmill of the NEJ type," *Transactions of the Central Institute for Aero-hydrodynamics of Moscow*, vol. 1, p. 57, 1920.

[7] G. A. Van Kuik, "The Lanchester–Betz–Joukowsky limit," *Wind Energy: An International Journal for Progress and Applications in Wind Power Conversion Technology*, vol. 10, no. 3, pp. 289–291, 2007.

[8] H. Glauert, *The elements of aerofoil and airscrew theory.* Cambridge University Press, 1983.

[9] N. Joukowsky, "Vortex Theory," *Trudy Otdeleniya Fizicheskikh Nauk Obshchestva Lubitelei Estestvoznaniya*, vol. 16, pp. 1–31, 1912.

[10] A. Ning, G. Hayman, R. Damiani, and J. M. Jonkman, "Development and validation of a new blade element momentum skewed-wake model within AeroDyn," in *33rd Wind Energy Symposium*, 2015, p. 0215.

[11] M. O. Hansen, *Aerodynamics of wind turbines.* Routledge, 2015.

[12] C. Lock, H. Bateman, and H. Townend, *Experiments to Verify the Independence of the Elements of an Airscrew Blade.* HM Stationery Office, 1924.

[13] T. Burton, D. Sharpe, N. Jenkins, and E. Bossanyi, *Wind energy handbook.* Wiley Online Library, 2001, vol. 2.

[14] W. Timmer and R. Rooij, "Summary of the Delft University Wind Turbine Dedicated Airfoils," *Journal of Solar Energy Engineering-transactions of The Asme - J SOL ENERGY ENG*, vol. 125, 01 2003.

[15] C. Bak, "Aerodynamic design of wind turbine rotors," in *Advances in Wind Turbine Blade Design and Materials.* Elsevier Inc., 1 2013, pp. 59–108.